Diffusion MRI for tumor microstructure imaging using VERDICT modeling

Department of Medical Radiation Sciences

Institute of Clinical Sciences

Sahlgrenska Academy, University of Gothenburg

UNIVERSITY OF GOTHENBURG

Gothenburg 2025

Cover illustration by Lena Lundholm

lukas.lundholm@gu.se

ISBN 978-91-8115-254-8 (PRINT)
ISBN 978-91-8115-255-5 (PDF)

Printed in Borås, Sweden 2025
Printed by Stema Specialtryck AB

If you never try, you'll never know
Coldplay (2005)

Diffusion MRI for tumor microstructure imaging using VERDICT modeling

Lukas Lundholm

Department of Medical Radiation Sciences, Institute of Clinical Sciences
Sahlgrenska Academy, University of Gothenburg
Gothenburg, Sweden

ABSTRACT

VERDICT is a method which uses a mathematical model that provides estimates of microstructural tumor tissue parameters based on diffusion-weighted MRI data. It is a promising imaging method for non-invasive *in vivo* evaluation of whole-tumor tissue. However, model assumptions may introduce systematic errors in parameter estimates.

The aim of this thesis was to assess the use of VERDICT for tumor tissue evaluation and investigate the impact of model assumptions on parameter estimates, as well as to develop and evaluate methods addressing accuracy issues related to some of these assumptions.

The standard clinical approach for evaluating tumor treatment response is by measuring changes in gross tumor volume. However, such changes can be slow, and methods sensitive to microstructural changes may detect response earlier. Paper I investigates the use of VERDICT parameters for radiation treatment response assessment and shows that early parameter changes correlate with treatment outcome.

Histological analysis remains the gold standard for assessing tumor microstructure, but tumor heterogeneity limits biopsy representativeness. Paper II explores the use of VERDICT for whole-tumor tissue classification as a potential complement to histology. The work shows that multidimensional cluster analysis of VERDICT parameters enables classification of distinct tumor tissue types.

Model assumptions can introduce systematic errors in parameter estimates. Paper III investigates the effect of assumptions related to extracellular–extravascular diffusion and presents a Monte Carlo-based model which explicitly accounts for diffusion time dependence. Paper IV investigates the impact of including compartment-specific T2 relaxation in the model, in contrast to uniform T2 relaxation across compartments as assumed in conventional VERDICT. These works show that model assumptions can significantly influence parameter estimates and present methods to mitigate their effects.

In conclusion, the results of this thesis highlight the importance of accurate model assumptions in VERDICT, and demonstrate the model's potential for non-invasive, whole-tumor evaluation of tumor tissue in various applications.

Keywords: cancer, histology, Monte Carlo, radiation therapy, treatment response, clustering, biophysical modeling

ISBN: 978-91-8115-254-8 (PRINT)
ISBN: 978-91-8115-255-5 (PDF)

POPLÄRVETENSKAPLIG SAMMANFATTNING

Molekyler i biologisk vävnad rör sig ständigt på ett till synes slumpmässigt sätt, drivet av värmeenergi. Detta fenomen kallas *diffusion* och med en magnetkamera (MR) kan man ta bilder som är känsliga för denna typ av mikroskopisk rörelse. Denna känslighet kan utnyttjas för att ta fram parametrar som speglar vävnadens mikrostruktur – som till exempel cellradie och intracellulär volym, direkt kopplat till celltäthet. I denna avhandling studeras en sådan metod – VERDICT – som utvecklats särskilt för att undersöka mikrostrukturen i cancervävnad.

Cancerdiagnostik är viktig både i det inledande skedet, för att välja rätt behandling, och under behandlingen, för att utvärdera dess effekt. Vid strålbehandling följs ofta tumörens storlek för att avgöra behandlingseffekten. Dessa storleksförändringar kan dock dröja, och föregås av vävnadsförändringar på mikroskopisk nivå. I denna avhandling undersöktes användandet av VERDICT för att mäta just dessa tidiga förändringar. Resultaten i denna avhandling visar på förändringar i bland annat intracellulär volym redan efter tre dagar, som dessutom speglade senare behandlingsrespons. Resultaten visade också att VERDICT kan användas för att klassificera olika typer av tumörvävnad genom att väga samman komplementär information, i detta fall intracellulär volym och cellradie.

VERDICT bygger på en modell av hur MR-signalen ser ut för en viss mikrostruktur och MR-bildtagning. Modellering innebär alltid en förenkling av verkligheten, så även för VERDICT. I denna avhandling visas att förenklande antaganden som vanligtvis görs för VERDICT, kopplat till diffusionen omkring celler och till vävnadens magnetiska egenskaper, kan orsaka systematiska fel i estimaten på mikrostruktur som tas fram (cellradie, mm.). För att minska dessa fel undersöktes och utvecklades metoder som gör det möjligt att analysera signalen utan att förlita sig på dessa antaganden.

Sammanfattningsvis visar avhandlingen att VERDICT-metoden har potential att bidra med värdefull information inom flera delar av cancerdiagnostiken, och presenterar metoder som förbättrar VERDICT-metodens möjligheter att korrekt bestämma tumörvävnadens mikrostruktur.

LIST OF PAPERS

This thesis is based on the following studies, referred to in the text by their Roman numerals.

I. **VERDICT MRI for radiation treatment response assessment in neuroendocrine tumors.**
Lundholm L, Montelius M, Jalnefjord O, Forssell-Aronsson E, Ljungberg M.
NMR in Biomedicine, 2022; 35(6):e4680

II. **Cluster analysis of VERDICT MRI for cancer tissue characterization in neuroendocrine tumors.**
Lundholm L, Montelius M, Jalnefjord O, Schoultz E, Forssell-Aronsson E, Ljungberg M.
NMR in Biomedicine, 2025; 38 (6):e70050

III. **A Monte Carlo-derived model of extracellular diffusion in solid tumors.**
Lundholm L, Montelius M, Jalnefjord O, Forssell-Aronsson E, Ljungberg M.
Manuscript

IV. **Effect of echo time on VERDICT MRI parameter estimation in brain tumors.**
Lundholm L, Jalnefjord O, Montelius M, Laesser M, Olsson Bontell T, Corell A, Jakola AS, Björkman-Burtscher I, Ljungberg M.
Manuscript

RELATED PRESENTATIONS

Early assessment of external beam radiotherapy response in an animal model of small-intestine neuroendocrine tumour (GOT1) using VERDICT modelling of diffusion MR data
Lundholm L, Montelius M, Jalnefjord O, Shubbar E, Swanpalmer J, Forssell-Aronsson E, Ljungberg M.
Annual Scientific Meeting ESMRMB 2019 Rotterdam, the Netherlands

VERDICT and kurtosis modelling of diffusion MRI for early assessment of radiotherapy response in a model of human neuroendocrine tumour
Lundholm L, Montelius M, Jalnefjord O, Shubbar E, Forssell-Aronsson E, Ljungberg M.
Annual Meeting ISMRM 2020 Virtual meeting

Repeatability of VERDICT diffusion MRI in a model of human neuroendocrine tumour
Lundholm L, Montelius M, Jalnefjord O, Forssell-Aronsson E, Ljungberg M.
Annual Meeting ISMRM 2021 Virtual meeting

VERDICT MRI for estimation of intracellular volume fraction and cell radius: comparison with histology in a mouse model of neuroendocrine tumor
Lundholm L, Montelius M, Jalnefjord O, Forssell-Aronsson E, Ljungberg M.
Joint Annual Meeting ISMRM-ESMRMB 2022 London, UK

Cluster analysis of VERDICT MRI for identification of tumor subregions with distinct histological features
Lundholm L, Montelius M, Jalnefjord O, Forssell-Aronsson E, Ljungberg M.
Annual Meeting ISMRM 2023 Toronto, Canada

Monte Carlo simulations of diffusion time and tortuosity effects on the extracellular signal: implications for VERDICT MRI model fitting in solid tumors
Lundholm L, Montelius M, Jalnefjord O, Forssell-Aronsson E, Ljungberg M.
Annual Scientific Meeting ESMRMB 2024 Barcelona, Spain

ABBREVIATIONS

ADC	Apparent Diffusion Coefficient
DKI	Diffusion Kurtosis Imaging
DNN	Deep Neural Network
dMRI	Diffusion Magnetic Resonance Imaging
EES	Extracellular-Extravascular Space
f_x	Signal fraction of x, e.g. f_{EES}
GMM	Gaussian Mixture Model
IC	Intracellular
IVIM	Intravoxel Incoherent Imaging
MC	Monte Carlo
PGSE	Pulsed Gradient Spin Echo
R	Cell radius
RF	Radiofrequency
ROI	Region of interest
SNR	Signal-to-noise ratio
T_D	Effective diffusion time
TE	Echo Time
TR	Repetition time
VASC	Vascular

VERDICT	Vascular, Extracellular and Restricted Diffusion for Cytometry in Tumors
Δ	Gradient separation time
δ	Gradient duration

Contents

1 INTRODUCTION

Molecular diffusion refers to the seemingly random microscopic motion of molecules, known as Brownian motion, driven by the thermal energy of a system. When this motion occurs within a magnetic field gradient, the phases of nuclear spins of atoms in the molecules become dispersed, resulting in attenuation of the magnetic resonance (MR) signal [1]. By incorporating an MR imaging (MRI) readout sequence, it is possible to acquire images with a diffusion-weighted signal contrast – a method known as diffusion MRI (dMRI) [2]. In a self-diffusing system, i.e. molecular motion within a specific medium, such as water, the diffusion can be described quantitatively using a diffusion coefficient [3]. Quantifying water diffusion in biological tissue is of particular interest due to its potential sensitivity to microstructural changes associated with pathology. Additionally, the high abundance of water molecules in biological tissue leads to a strong MR signal when the MRI system is tuned to detect hydrogen. However, water diffusion *in vivo* rarely reflects pure self-diffusion, as it is affected by barriers like cell membranes, and the diffusion-weighted MR signal can also be affected by other motions such as blood flow. To address this complexity, the MR signal can be modeled as originating from multiple microstructural compartments, each with distinct diffusion characteristics. These so-called biophysical dMRI models aim to provide a more realistic representation of tissue microstructure [4]. One such model, developed specifically for tumor characterization, is VERDICT (Vascular, Extracellular, and Restricted Diffusion for Cytometry in Tumors) [5]. VERDICT models the signal as originating from three compartments: (1) a vascular compartment, representing both self-diffusion and blood flow within vessels; (2) an intracellular compartment, characterized by restricted diffusion within cells; and (3) an extracellular-extravascular compartment, where diffusion is considered hindered but not fully restricted.

Model fitting in dMRI is commonly described as an inverse problem, in which a biophysical model is fitted to the measured diffusion-weighted signal to estimate underlying microstructural parameters. In the case of the VERDICT model, these parameters include, for example, the intracellular volume fraction and cell radius. Such estimates have demonstrated potential in applications such as tumor grading and treatment monitoring [6–8], and have shown correspondence with histological analysis of tumor tissue [5,7,9].

Tumors are often heterogeneous, comprising regions of, e.g., viable, proliferative cancer cells or necrosis containing non-viable cells. Characterization of tumor tissue is an important part of cancer diagnostics for tumor grading and selection of appropriate treatment strategies. Currently, the clinical gold standard for assessing tumor tissue microstructure remains histological analysis of biopsy samples [10,11]. However, biopsy procedures are often resource-intensive, carry procedural risks for the patient, and may not fully capture tumor heterogeneity due to spatial sampling limitations [12,13]. In contrast, dMRI methods like VERDICT shows potential as a non-invasive alternative that can generate parameter maps across the entire tumor volume. As such, dMRI could serve as a valuable complement to histology, potentially offering new insights into tissue microstructure and tumor biology.

VERDICT provides estimates of multiple microstructural parameters, and analyzing each parameter in isolation may limit the ability to capture complementary information or underlying patterns that can aid in, e.g., tissue classification. Cluster analysis offers a way to integrate information across multiple parameters, highlighting multidimensional relationships that may not be apparent when analyzing each parameter separately. In multiparametric MRI, clustering techniques have shown promise in differentiating between various tumor tissue types [14,15], and they represent a promising, yet unexplored, approach for analyzing VERDICT data as well.

Microstructural parameters derived from dMRI models such as VERDICT also hold promise for assessing tumor response to treatment. The standard clinical approach typically involves measuring changes in gross tumor volume [16]. However, such volumetric changes often occur as a late response to therapy, and treatment-induced increases in tumor volume can lead to misinterpretation of the actual treatment effect [17,18]. In contrast, changes in the tumor microstructure, such as cell shrinkage during apoptosis [19], may precede observable changes in tumor size. As such, VERDICT may offer a means of detecting these earlier microstructural changes, allowing earlier assessment of treatment effect.

Biophysical dMRI models, such as VERDICT, are often complex with multiple free parameters which can make parameter estimation challenging. To improve robustness, simplifying assumptions are often introduced; however, they may come with the cost of reduced accuracy [20]. A common assumption in VERDICT is that all compartments share the same T2 relaxation time, i.e., the rate at which the MR signal decays following excitation. If the

compartments exhibit different T2 relaxation times, this assumption will introduce a bias in the parameter estimates [21]. Furthermore, the microstructure of the extracellular–extravascular space is inherently complex. In the VERDICT model, diffusion within this compartment is typically modeled under the assumption of Gaussian diffusion – that is, molecular displacement over time is assumed to follow a Gaussian distribution. This assumption is based on the idea that, given sufficiently long diffusion times during the diffusion-sensitizing part of the MRI sequence, the signal is no longer sensitive to fine-scale microscopic features of the microstructure and instead reflects an effective, coarse-grained description of the tissue [22]. However, under typical experimental conditions, this assumption may not hold [23]. As a result, a Gaussian model may introduce estimation biases that are dependent on both the MRI sequence parameters and the specific tissue microstructure under investigation [23]. Understanding the nature and extent of these biases is essential for accurately interpreting VERDICT-derived parameters and guiding future optimization of the model.

Due to the complexity of the extracellular–extravascular microstructure, analytical modeling of this compartment is challenging. Monte Carlo (MC) simulations provide an alternative approach by modeling diffusion as a stochastic process, where molecules are represented as random walkers [24]. These simulations can be adapted to any diffusion-sensitizing MRI sequence and microstructural geometry, allowing precise control over both MRI sequence parameters and the spatial arrangement of diffusion barriers. MC simulations are commonly used to validate analytical models and theoretical assumptions [24]. However, they also have potential to serve as a basis for developing empirical, simulation-derived signal models.

2 AIMS

The overall purpose of this thesis was to evaluate and improve the non-invasive, MR-based method VERDICT for tumor characterization and treatment assessment.

The specific aims were to evaluate the use of multiparametric VERDICT analysis for:

- detection of early radiation treatment response (Paper I)
- classification of tumor voxels as distinct tissue types (Paper II)

and to evaluate and address systematic errors originating from VERDICT model assumptions related to:

- diffusion time-dependence in extracellular-extravascular space (Paper III)
- compartment-specific T2 relaxation (Paper IV)

3 DIFFUSION MRI MODELING

3.1 THE DIFFUSION MRI SIGNAL

The first and most widely used MRI sequence to provide a diffusion-weighted MRI (dMRI) signal is the pulsed gradient spin echo (PGSE, Figure 1) sequence, originally introduced by Stejskal and Tanner [25]. The fundamental principle of the PGSE sequence is that, after excitation of spins using a radiofrequency (RF) pulse, a magnetic field gradient, often referred to simply as a "gradient", is applied across the region of interest. This gradient causes phase dispersion among the spins, resulting in attenuation of the transverse magnetization. A second, refocusing gradient is then applied to rephase the spins and recover the signal. However, this refocusing is only fully effective for stationary spins. For spins in motion, such as those undergoing diffusion, the refocusing will be incomplete, resulting in a signal attenuation that reflects the characteristics of the spin motion. In the case of free diffusion, where no barriers or non-diffusional motion are present, the dMRI signal, S, can be described by the mono-exponential expression:

$$S = S_0 e^{-bD} \tag{1}$$

where S_0 is the signal without diffusion weighting (i.e., with no diffusion gradients applied), D is the diffusion coefficient (expressed in units of, e.g., μm²/ms), and b, commonly referred to as the b-value [2], is a parameter that reflects the degree of diffusion sensitization, or "weighting", on the signal, given by:

$$b = \gamma^2 G^2 \delta^2 \left(\Delta - \frac{\delta}{3}\right) \tag{2}$$

where γ is the gyromagnetic ratio, G is the gradient strength, Δ is the gradient separation time, and δ is the gradient duration. The specific expression for the b-value depends on the chosen diffusion-weighting sequence and is given here for the PGSE sequence. A refocusing RF pulse is applied between the two diffusion gradients, generating a spin echo at the echo time (TE), where signal readout is performed. Importantly, diffusion weighting is applied only along the direction of the applied diffusion gradients. To probe motion in multiple directions using PGSE, the acquisition must be repeated with different diffusion sensitizing gradients directions. This relatively straightforward yet

powerful sequence has laid the foundation for the entire field of diffusion MRI, enabling non-invasive measurement of molecular motion in biological tissues. As explored in this thesis, it may also be used to provide estimates of tissue microstructure parameters.

Two additional key concepts are introduced here. First, the effective diffusion time (T_D) represents the effective duration over which spins diffuse during the diffusion-sensitizing period of the sequence. For a PGSE sequence, T_D is defined as [25]:

$$T_D = \Delta - \frac{\delta}{3} \tag{3}$$

Second, the effective diffusion length L_D, referring to the root mean square displacement of spins, defined as [3]:

$$L_D = \sqrt{2nDT_D} \tag{4}$$

where n is the number of spatial dimensions. Both of these concepts are important in the context of dMRI, as they determine the extent to which the surrounding microstructure is explored by the spins during a dMRI sequence.

3.2 SIGNAL REPRESENTATIONS

To extract quantitative information from the diffusion-weighted signal, a mathematical expression describing the signal attenuation, referred to as a signal representation, can be fitted to signal data acquired using varying gradient configurations [4]. This fitting process represents an inverse problem, where the goal is to estimate the parameters of the chosen signal representation. The simplest and most commonly used signal representation estimates a single parameter: the Apparent Diffusion Coefficient (ADC) [2], expressed as:

$$S = S_0 e^{-bADC} \tag{5}$$

This expression closely resembles Equation (1), which describes signal attenuation under free diffusion. Under such conditions, the ADC equals the intrinsic diffusion coefficient. However, in biological tissues, characterized by complex microstructural environments, ADC reflects not only the intrinsic diffusivity but also the influence of structural barriers (e.g., cell membranes) and vascular flow. It is for this reason that the term *apparent* is used.

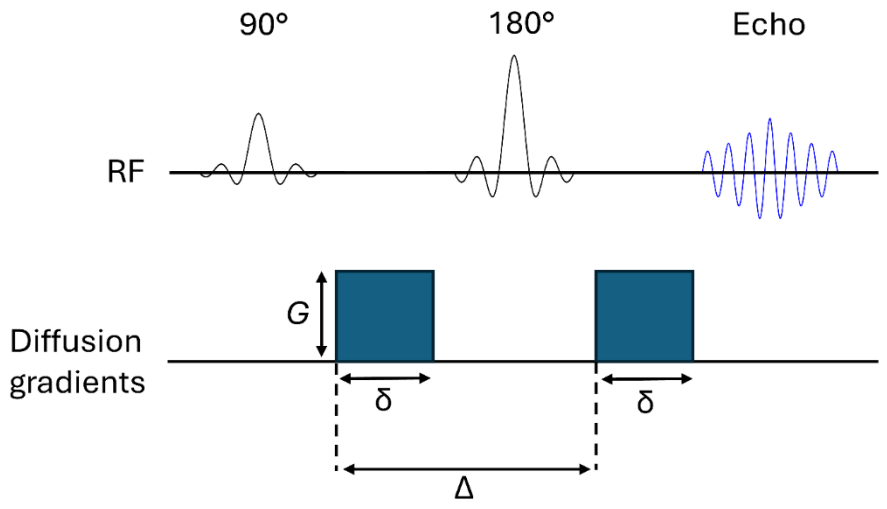

Figure 1. Illustration of the pulsed gradient spin echo (PGSE) sequence used to sensitize the MRI signal to water molecule motion. The sequence follows these steps: (1) a 90° radiofrequency (RF) pulse excites the spins; (2) a diffusion gradient induces phase dispersion; (3) a 180° RF pulse inverts the spin phases; (4) a second diffusion gradient attempts to rephase the spins; and (5) signal readout is performed at the spin echo. The degree of diffusion sensitization is determined by the gradient strength (G), gradient duration (δ), and gradient separation time (Δ). Spins in motion during the diffusion sensitization period ($\Delta + \delta$) do not fully rephase, resulting in a signal attenuation that reflects the motion characteristics of the system

Equation (1) is derived under the assumption of Gaussian diffusion, meaning that the probability distribution of a spin's displacement follows a normal distribution. In biological tissue, however, the presence of structural barriers causes deviations from Gaussian behavior. The extent of this deviation can be quantified by the dimensionless kurtosis metric, K, leading to the following extended signal representation, as presented by Jensen et al. [26]:

$$S = S_o e^{-bD_k + \frac{b^2 D_k^2 K}{6}} \tag{6}$$

where D_k can be interpreted as the kurtosis-corrected diffusion coefficient. In the case of Gaussian diffusion, $K = 0$, while a positive kurtosis ($K > 0$) reflects

heterogeneous diffusivity resulting from complex tissue microstructure. Estimating D_k and K by fitting this expression to the diffusion-weighted signal is referred to as Diffusion Kurtosis Imaging (DKI). Importantly, like the ADC, both D_k and K are apparent parameters and typically depend on the specific gradient configuration used in the dMRI sequence.

3.3 BIOPHYSICAL MODELS

While signal representations are mathematical expressions that aim to describe the dMRI signal in a descriptive manner, biophysical models go one step further by attempting to explain the signal based on underlying biophysical and microstructural properties of the tissue [4]. The central concept in biophysical modeling is that different tissue compartments exhibit distinct water motion characteristics, leading to differences in their signal contributions that can be disentangled through model fitting. Biophysical models typically combine multiple compartment-specific models, each describing the behavior of water molecules in a specific tissue environment [27–29]. One such compartment is the vascular (VASC) compartment, which includes water motion driven by both diffusion and incoherent vascular flow within blood vessels. One commonly used model for the VASC signal, S_{VASC}, is derived from the original work by Le Bihan et al. [28], and commonly expressed as:

$$S_{VASC} = e^{-bD^*} \tag{7}$$

where D^* represents the pseudo-diffusion coefficient which incorporates the combined effects of molecular diffusion and blood flow within blood vessels [30]. Ahlgren et al. proposed a VASC compartment model that aims to disentangle the contributions of flow and diffusion by incorporating velocity dispersion, v_d [31]. The model expresses the VASC signal as:

$$S_{VASC} = e^{-bD_b} e^{-\alpha^2 v_d^2} \tag{8}$$

where D_b is the diffusion coefficient of water in blood and α, the flow encoding factor, is given by the following expression for a PGSE sequence:

$$\alpha = \gamma G \delta \Delta \tag{9}$$

Astrosticks is another model used to describe the VASC compartment. It models water molecule motion as one-dimensional diffusion within randomly oriented, zero-radius cylinders, representing ideal blood vessel segments. The

full model expression and derivation are presented in Panagiotaki et al. [32]. The two latter VASC models assume that blood flow occurs within randomly oriented, straight vessel segments. However, whether this assumption holds likely depends on T_D, as a longer T_D allows more time for water molecules flowing through capillaries to change direction during the diffusion sensitization period [33].

In solid tumors, the intracellular (IC) signal, S_{IC}, can be modeled as restricted diffusion, where water molecules are confined within a finite IC space. The geometry of this restriction may vary within and between tumor types, but spherical restriction is commonly assumed. The spherical restriction model was originally derived by Murday and Cotts [34], with a more complete analytical derivation later presented by Neuman [35]. This model depends on several parameters: the intracellular diffusion coefficient (D_{IC}), cell radius (R), as well as G, δ, and Δ, leading to a distinct diffusion time-dependence.

The extracellular-extravascular space (EES) signal, S_{EES}, is typically modeled using a Gaussian assumption [5,29,36], similar to Equation (1):

$$S_{EES} = e^{-bD_{EES}} \tag{10}$$

where D_{EES} is the effective (or apparent) diffusion coefficient of the EES. This model assumes that diffusion is hindered rather than restricted, and that the acquisition occurs in the long diffusion time regime, also referred to as the tortuosity limit, where the signal becomes time-independent [37]. This assumption is further discussed in Chapter 5.2.

By combining the individual compartment signal models, complete biophysical models can be formulated to model the full dMRI signal. One such model is IVIM (Intravoxel Incoherent Motion), which aims to estimate both perfusion- and diffusion-related tissue parameters [28]. The IVIM signal model is given by:

$$S = S_0[f_{VASC}S_{VASC} + (1 - f_{VASC})S_{EV}] \tag{11}$$

where f_{VASC} represents the signal fraction of the vascular compartment, commonly referred to as the perfusion fraction, and S_{EV} is the extravascular signal. Because the motion associated with perfusion is much faster than molecular diffusion, the VASC signal tends to attenuate rapidly with increasing b-values. Consequently, IVIM applications typically emphasize

acquisitions at low b-values to capture perfusion-related signal variations. At low b-values, the effects of kurtosis are minimal and, as such, S_{EV} is typically modeled as Equation (10).

VERDICT (Vascular, Extracellular, and Restricted Diffusion for Cytometry in Tumors) is a biophysical model structurally similar to IVIM, but with a more detailed representation of the extravascular space. Specifically, it separates the extravascular signal into two distinct compartments: IC and EES. The model was originally presented by Panagiotaki et al. [5] and can be expressed as:

$$S = S_0[f_{IC}S_{IC} + f_{EES}S_{EES} + f_{VASC}S_{VASC}] \quad (12)$$

where f_{IC} and f_{EES} represent the signal fractions of the IC and EES compartments, respectively. The signal fractions are constrained to sum to one, so f_{VASC} does not need to be independently estimated during model fitting, but can instead be calculated as:

$$f_{VASC} = 1 - f_{IC} - f_{EES} \quad (13)$$

The exact analytical expressions used to model each compartment signal can be chosen based on the specific microstructural characteristics of the tissue under investigation. However, the papers included in this thesis use the compartment models presented in this chapter. To ensure strong contrast between compartment-specific signals, the VERDICT model is typically fitted to dMRI signal data acquired across a wide range of b-values and T_D. It is important to note that the modeling approach presented here assumes that there is no exchange of water between compartments or that T_D is short enough to make compartment exchange effects negligible, although this assumption may not always hold [38]. Many other biophysical models have been proposed for various tissue types. For solid tumors, two examples are IMPULSED (Imaging Microstructural Parameters Using Limited Spectrally Edited Diffusion) [29] and POMACE (Pulsed and Oscillating Gradient MRI for Assessment of Cell Size and Extracellular Space) [36]. These models are conceptually similar to VERDICT but incorporate combined measurements using PGSE and oscillating gradient spin echo (OGSE) sequences to include shorter T_D [39]. For brain tissue, a range of biophysical models have also been developed. Notable examples include NODDI (Neurite Orientation Dispersion and Density Imaging) [27] and CHARMED (Composite Hindered and Restricted Model of Diffusion) [40]. A key distinction in modeling brain tissue is the need to account for signal dependence on spatial direction, which enables the

characterization of anisotropic diffusion in white matter where water diffusion predominantly follows the orientation of axonal fibers [41].

3.4 MONTE CARLO SIMULATIONS

Signal representations and biophysical models provide analytical expressions that describe the dMRI signal and can be used to simulate signal values based on specified parameter inputs. An alternative to these analytical approaches is the use of Monte Carlo (MC) simulations [24]. In this technique, diffusing water molecules, or spins, are represented by random walkers moving through a digital simulation space. At each time step of duration *dt*, each walker takes a step of length

$$L_{step} = \sqrt{2 \cdot n \cdot D_{int} \cdot dt} \tag{14}$$

in a random direction, where D_{int} is the intrinsic diffusion coefficient, and n is the number of spatial dimensions [42]. An illustration of random walks simulating diffusion is shown in Figure 2. Each walker has an associated phase, and during each step, the walker accumulates a phase shift due to the presence of a time-varying diffusion-sensitizing magnetic field gradient, given by the specific dMRI sequence used. After the full sequence duration, the accumulated phases of all walkers are combined to calculate the normalized diffusion-weighted signal. These simulations can be performed for any configuration of gradient strength and timing, and barrier geometries can be included in the simulation space to mimic hindering or restricting tissue microstructure, such as packed spheres to represent cells. The MC-technique is thus a powerful tool for studying dMRI signal behavior under complex conditions and has been widely used for validating dMRI models [24]. Paper III investigates the use of MC simulations to directly function as biophysical models to estimate microstructural parameters from measured dMRI signals. This approach is further discussed in Chapter 5.2.

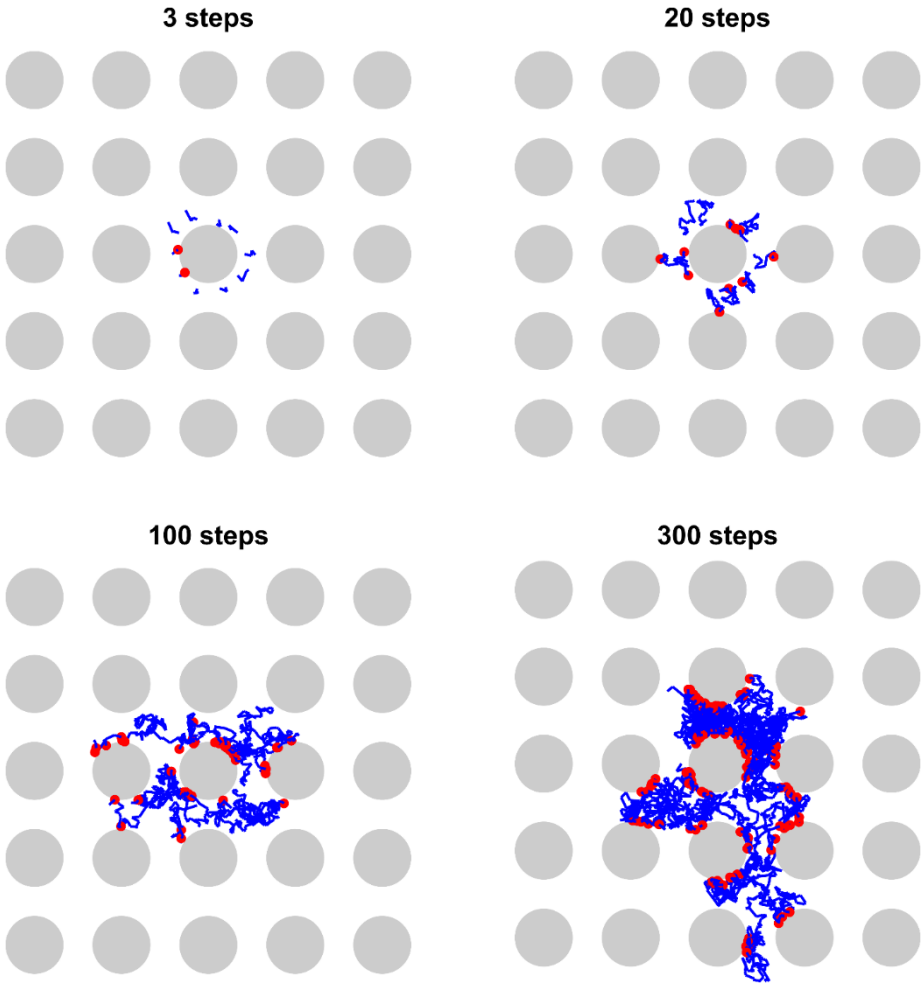

Figure 2. Illustration of Monte Carlo simulations in dMRI. Diffusion is simulated using random walkers, each taking steps in random directions with step length determined by the intrinsic diffusion coefficient. Increasing the number of steps simulates increasing diffusion times (T_D). The figure shows paths (blue lines) of ten walkers in a 2D space with circular restrictions. Red markers indicate interactions with barriers. As T_D increases, so does the number of interactions, leading to a reduced effective diffusion coefficient

4 APPLICATIONS OF VERDICT

This chapter is mainly related to Papers I and II. These works were conducted using a mouse model of small-intestine neuroendocrine tumor.

In Paper I, VERDICT was evaluated for its potential to assess early response to radiation treatment by examining the correlation between model parameters and volume-based treatment response. The explanatory value of VERDICT was also assessed through a linear regression analysis combining multiple VERDICT parameters. For comparison, results were also evaluated against those obtained using ADC, IVIM, and DKI.

In Paper II, clustering of VERDICT parameters using a Gaussian mixture model was used to classify tumor voxels into distinct tissue types. The resulting VERDICT-based probability maps were compared with histological data.

4.1 TUMOR TISSUE CHARACTERIZATION

Accurate characterization of tumor tissue is essential for proper classification and grading, both of which play a critical role in determining tumor aggressiveness and guiding treatment decisions. The gold standard for tumor microstructural characterization in clinical practice is histological analysis of biopsy samples obtained through surgery. Histological analysis forms a foundational component of key tumor classification systems, including the World Health Organization (WHO) criteria for brain tumors and prostate cancer [10,11]. Unlike histological analysis, VERDICT offers a non-invasive approach for estimating microstructural parameters across the entire tumor volume. As such, VERDICT is a promising method for providing complementary and spatiotemporal information to conventional tissue analysis. Several studies have demonstrated the potential of VERDICT for tumor classification and diagnostic stratification in both prostate and brain cancers [6,7,43–45]. However, due to the large number of parameters estimated by VERDICT, more advanced multiparametric data analysis techniques, such as cluster analysis, may be needed to fully leverage the information contained within the estimated parameters. Furthermore, validation of these imaging-derived parameters against histological references is important to ensure their biological relevance and clinical reliability.

4.1.1 CLUSTER ANALYSIS

Cluster analysis refers to a set of unsupervised methods used to partition data into subgroups based on similarities in one or more dimensions. These methods are particularly useful for identifying underlying patterns in multidimensional datasets, such as parameters derived from VERDICT analysis. Among the most commonly used techniques is k-means clustering, which partitions data into k clusters, where k is predefined, by minimizing the squared Euclidean distance between data points and the mean of their assigned cluster. Several studies have applied k-means clustering to MRI data in cancer research, including tasks such as differentiating benign from malignant tissue and tumor segmentation [46–49]. While k-means is simple and computationally efficient, it performs poorly when clusters overlap, differ greatly in size, or deviate from spherical shapes. More advanced methods have been developed to address these challenges. For example, Hierarchical Density-Based Spatial Clustering of Applications with Noise (HDBSCAN) does not assume spherical clusters and can identify clusters of varying densities and shapes, while also automatically determining the number of clusters and labeling outliers as noise [50,51]. Spectral clustering offers another alternative by transforming the data into a lower-dimensional space where the underlying structure may become more separable, enabling the detection of clusters with overlapping features or irregular boundaries [52]. However, both HDBSCAN and spectral clustering typically require more careful tuning of hyperparameters and may produce results that are less straightforward to interpret compared to the simplicity of k-means.

Another approach to clustering is fitting a Gaussian Mixture Model (GMM) to the data. As with k-means clustering, GMM requires predefining the number of clusters (k). The method then attempts to model the data as a mixture of k Gaussian distributions. Each distribution is characterized by three key parameters: the mean, which represents the center of the cluster; the covariance matrix, which defines the shape, spread, and orientation of the cluster (and reduces to a scalar variance in the one-dimensional case); and the weight, which controls the relative contribution of each Gaussian component to the overall distribution. Once the model is fitted, each data point is assigned a probability of belonging to each cluster, enabling a soft classification. Because GMM is based on the assumption that clusters follow a normal distribution, it is particularly well-suited for data where this assumption is expected – a common scenario in many biological systems. Several recent studies have

demonstrated the ability of GMM to capture spatial tumor heterogeneity in MRI data [15,53–55].

A key advantage of GMM over k-means is that it performs soft clustering, assigning each data point a probability of belonging to every given cluster. This is particularly useful in cases where clusters overlap or, in the context of MRI, when voxels contain a mixture of different tissue types. In contrast, k-means performs hard clustering, where each point is assigned to a single cluster only. Additionally, GMM accounts for the scale and shape of each dimension individually through its covariance matrix, making it more flexible when handling features with different units or distributions. Figure 3 shows an example where GMM performs better than k-means in separating elongated clusters in close proximity.

In Paper II, a GMM was applied to VERDICT parameter estimates from the GOT1 tumor model [56]. The number of clusters (k) was predefined as three, based on visual inspection of histological sections where three distinct tissue types were identified: necrotic, fibrotic, and viable tumor tissue. The microstructural characteristics of these tissue types are further discussed in Section 4.2. Among the VERDICT parameters, f_{IC} and R showed the most potential for differentiating the tissue types based on correspondence with histological findings. Consequently, the three-cluster GMM was fitted to data in the two-dimensional parameter space defined by f_{IC} and R. The resulting soft clustering enabled the generation of probability maps indicating the likelihood of each voxel belonging to a specific tissue class. These maps demonstrated good spatial correspondence with histological data and highlighted the potential of GMM-based clustering for non-invasive tumor tissue classification using VERDICT. The three Gaussian components exhibited substantial overlap and elongated shapes, suggesting that GMM, due to its ability to model anisotropic and overlapping clusters, was likely well-suited for this application. The results also demonstrated that joint analysis of multiple VERDICT parameters improved tissue classification compared to analyzing parameters in isolation, highlighting the importance of multiparametric approaches to fully leverage the information contained in VERDICT data.

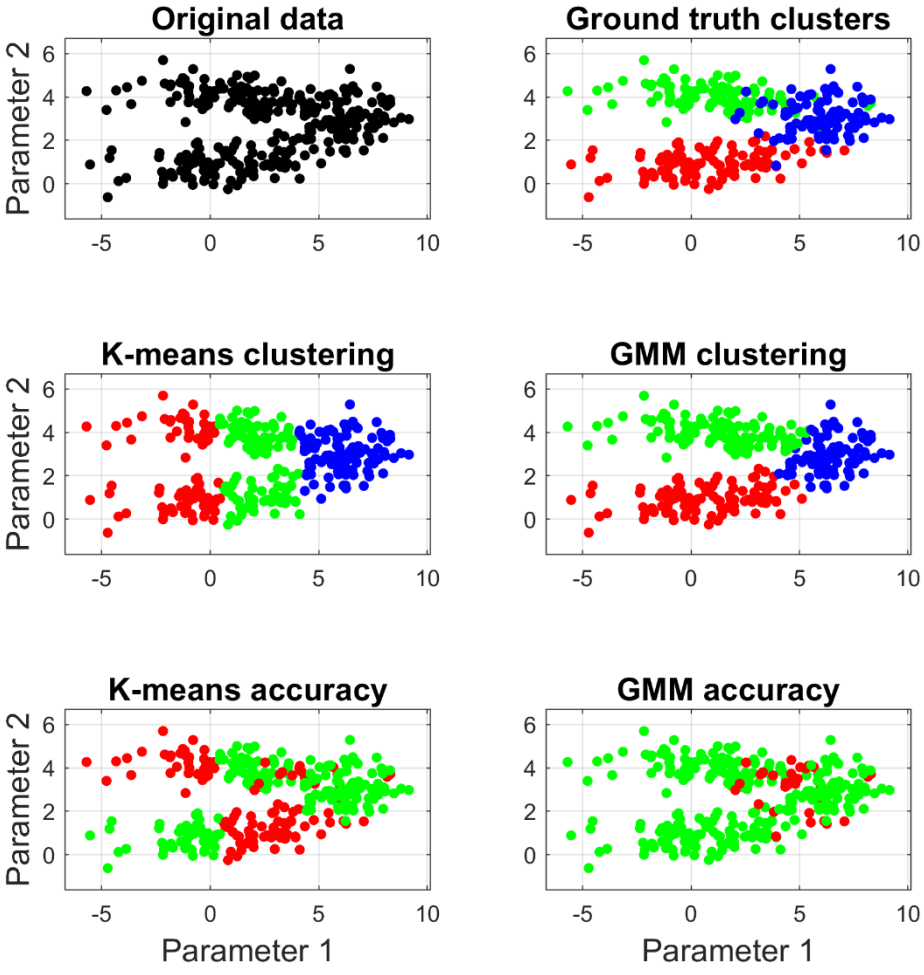

Figure 3. Comparison of the performance of a Gaussian Mixture Model (GMM) and k-means in a clustering scenario where two of the clusters are elongated and positioned close to one another. K-means misclassifies points due to its reliance on distance-based partitioning. GMM, by modeling the full covariance structure of each cluster, is therefore better suited to separate such anisotropic clusters

In Paper II, viable tumor tissue spatially corresponded best with the cluster characterized by high f_{IC}, while necrotic and fibrotic tissue corresponded to clusters with lower f_{IC}. This suggests that f_{IC} captures important microstructural differences that help distinguish viable from non-viable tissue. Previous studies have reported elevated ADC values in necrotic regions compared to viable tumor tissue [57–59], which is commonly attributed to reduced cell density, resulting in fewer barriers that hinder and restrict diffusion. The lower f_{IC} observed in the cluster associated with necrosis in Paper II aligns with these findings, as a reduced f_{IC} reflects decreased cell density. However, f_{IC} alone provided almost no discriminatory value between fibrosis and necrosis; these tissue types were primarily distinguished by differences in the R parameter. Specifically, necrotic tissue was associated with high R values, while fibrotic tissue was associated with lower R values. The elevated R observed in the necrotic regions is consistent with common features of necrotic cell death, including cell swelling and ultimately cell membrane rupture [60]. The biological interpretation of the low R in fibrotic regions remains less clear. Nevertheless, the findings in Paper II demonstrated that, among the VERDICT parameters, R plays an important role in differentiating fibrotic from necrotic tissue. It is also worth noting that another potential contributor to the low f_{IC} observed in the necrotic regions could be increased cell membrane permeability, which would increase the exchange rate between the intra- and extracellular compartments. Since the VERDICT model assumes fully restricted diffusion within the intracellular space, increased permeability may compromise the model's ability to accurately distinguish intracellular from extracellular diffusion [61]. Under such conditions, the diffusion-weighted signal may more closely reflect hindered rather than restricted diffusion, potentially explaining the observed reduction in f_{IC}.

Fitting models to dMRI signal data can help extract meaningful, quantitative parameters related to tissue microstructure, potentially offering more value than qualitative analysis of diffusion-weighted images alone. However, all model parameters ultimately originate from the information contained in the measured signal itself. This raises the question of whether model fitting is necessary, or whether direct analysis of the diffusion-weighted signal may suffice. With the rise of AI in medical imaging, it may be more effective to feed raw signal data directly into algorithms or neural networks [62–65]. In Paper II, this idea was briefly explored. Plotting signal intensities using a high b-value (3650 s/mm²) and long T_D against those using a lower b-value (933 s/mm²) and short T_D revealed separable clusters when the data were labeled according to histology-derived tissue classifications. These results suggest that

tissue classification may be feasible directly from the diffusion-weighted signal by using carefully selected acquisition parameters, thus avoiding model-related biases altogether. The findings also indicate that a small subset of the acquisitions may have contained most of the relevant information needed to distinguish tissue types. Acquiring only this subset of signal values would substantially reduce total scan time. However, direct analysis of the signal places strict demands on protocol standardization across scans, as such a method would be highly sensitive to acquisition parameters – especially when training neural networks.

4.1.2 HISTOLOGICAL VALIDATION

VERDICT aims to disentangle the information encoded in the dMRI signal to estimate parameters related to biophysical processes and tissue microstructure. However, as the model is a simplification of real tumor tissue and incorporates assumptions to improve robustness, validating the estimated parameters is essential to ensure their biological relevance and correct interpretation. The most common method for validating biophysical dMRI models is through comparison with histological analysis [66,67]. Histology involves the *ex vivo* examination of tissue, typically by cutting it into thin sections, staining it to highlight specific tissue features, and finally analyzing it under a light microscope. This enables visual inspection at the microscopic level and allows for the extraction of quantitative data, such as cell density, proliferation, and vascular integrity, through image analysis techniques. In addition, tissue can be classified using computational algorithms applied to digitized histological images. As previously outlined, histological analysis forms the foundation for tumor tissue evaluation in clinical practice and is integral to many tumor classification systems. Therefore, validating biophysical dMRI parameters against histology provides a direct link between model output and clinical standards. Several previous studies have demonstrated correlations between dMRI-derived biophysical model parameters and histologically derived features in tumors, including, for example, correlations between dMRI-estimated cell radius and the minimum Feret diameter of cells, i.e. the shortest distance between two parallel lines tangential to its boundary, among other microstructural metrics [68–73].

Despite histology being the most commonly used method for validating dMRI model parameters, a major limitation is that it provides information from *ex vivo* tissue, whereas MRI provides *in vivo* estimates. There are numerous tissue processing steps between MRI acquisition and histological analysis, each of

which can introduce distortions or artifacts. Following resection or biopsy, the tissue must first be fixated by, e.g., immersing it in a fixative solution, typically formalin, to prevent degradation and preserve cellular and extracellular structures. The fixed tissue is then typically embedded in a paraffin wax block to facilitate sectioning. However, because paraffin wax is hydrophobic, the tissue must first be dehydrated by gradually replacing its water content with alcohol through a series of alcohol baths. Once dehydrated and embedded, the tissue is sectioned into slices approximately 5 μm thick using a microtome. These thin sections are then stained with chemical dyes to provide color contrast between different tissue components. Finally, the stained sections are either examined under a light microscope or digitized using a whole-slide scanner for image analysis and storing.

A wide range of tissue staining techniques are available in histology, each providing different types of contrast depending on the target structures. Figure 4 shows examples of stained tumor tissue. The most commonly used stain is hematoxylin and eosin (HE), which provides strong visual contrast between common tissue components: hematoxylin stains cell nuclei dark purple, while eosin stains the cytoplasm and extracellular matrix in varying shades of pink. This combination enables clear visualization of basic tissue morphology. Masson's trichrome (MT) is another multicolor stain, particularly useful for visualizing connective tissue. Typically, in MT staining, collagen appears blue, cytoplasm is stained red, and nuclei take on a darker hue, providing good contrast in fibrotic tissues. Another common approach, called immunohistochemistry (IHC) is often used to visualize specific proteins within tissue sections. This method uses antibodies that bind to target antigens, resulting in a visible color change, often brown, at the site of binding. A commonly used IHC marker in tumor tissue analysis is Ki-67 staining, which binds to the Ki-67 protein expressed during the active phases of the cell cycle. Ki-67 staining thus serves as a marker for cellular proliferation and is particularly valuable for identifying regions of viable tumor cells.

During histological tissue processing, prior to staining, a number of artifacts may be introduced, such as tissue folding and ripples caused by vibrations of the microtome blade during sectioning. While some artifacts can be minimized through careful handling, others are inherent to the preparation process itself [74,75]. A particularly notable example is tissue shrinkage during fixation and dehydration, which can alter morphology both at the whole-tissue level and at the cellular scale, such as through cell shrinkage [76]. These morphological

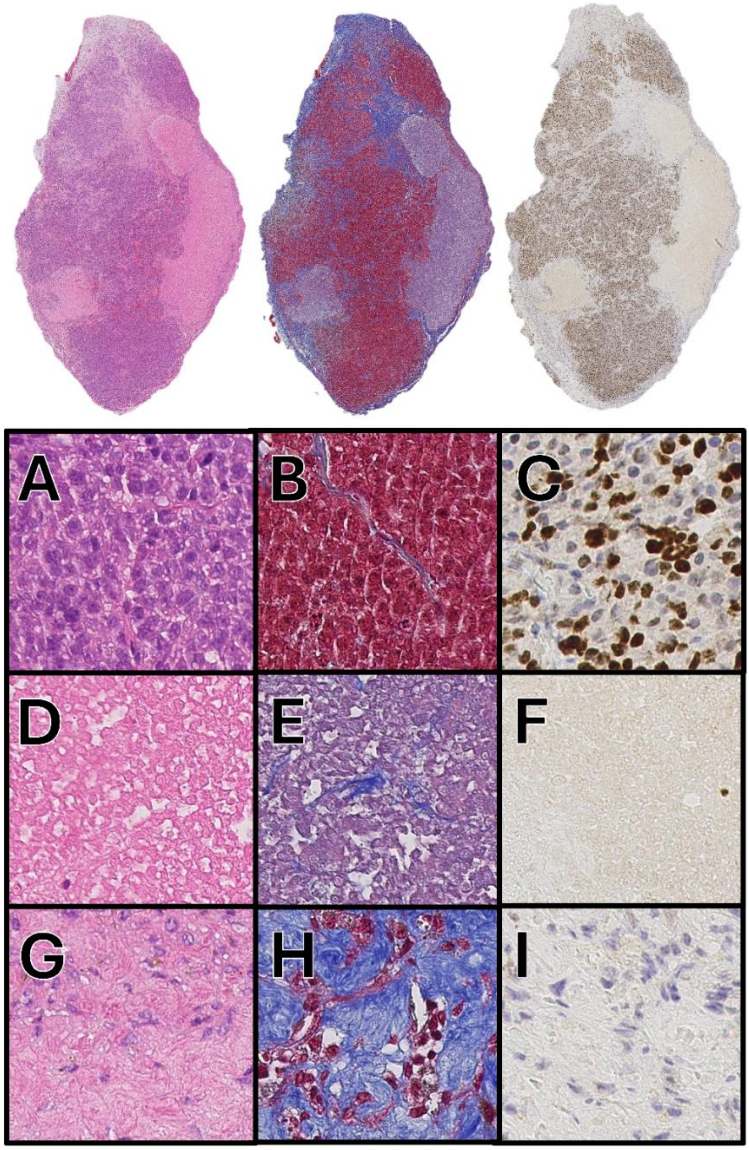

Figure 4. Examples of histological images from a tumor section. The upper panel shows whole-slide images or the tumor, while the lower panel presents enlarged regions. Stains include hematoxylin and eosin (left; A, D, G), Masson's trichrome (middle; B, E, H), and Ki-67 (right; C, F, I). The zoomed-in images in the lower panel illustrate different tissue types: viable (A–C), necrotic (D–F), and fibrotic (G–I) tumor tissue. Each stain highlights unique characteristics of the tissue

changes represent a significant limitation when using histological analysis to validate dMRI-derived microstructural parameters like cell size, as the original *in vivo* microstructure may be altered, making direct quantitative comparison challenging or misleading.

Histological methods produce images that are not only suitable for qualitative visual interpretation but can also be quantitatively analyzed, for example, by counting cells per unit area. More advanced analyses can be made by scanning stained tissue sections and processing them as digital images. Basic methods include thresholding across color components (e.g. RGB channels) to quantify pixels of specific colors, while more sophisticated approaches involve image transformations for extracting complex features. Figure 5 shows an example of cell segmentation applied to an HE-stained tumor tissue section. Machine learning methods can enable further analysis by identifying patterns based on features such as pixel intensity, texture, and edges, enabling classification of tissue types [77]. Digital image processing not only facilitates the detection of patterns that may be difficult to discern visually, but also supports high-throughput analysis through batch processing which is an important advantage given the time-intensive nature of manual quantification. At microscopic resolution, even small tissue sections may represent areas populated by thousands of cells, making manual analysis, such as cell counting, not only highly time-consuming but also often limited to small regions of interest, which may not fully capture the full tissue heterogeneity. Nevertheless, despite the efficiency of automated methods, it remains crucial to validate them against expert human interpretation to ensure biological relevance. A showcase of the supervised machine learning classification method used in Paper II is shown in Figure 6.

In Paper II, tumor tissue classification maps generated from the cluster analysis of VERDICT parameters were compared with histological sections to validate the classifications. Three distinct tissue types were identified in the histological data: necrotic, fibrotic, and viable tissue (Figure 4). Viable tissue was characterized by high cell density and the presence of proliferative cells, as indicated by positive Ki-67 staining. Fibrotic tissue was most clearly observed using MT staining, appearing as regions with stained collagen fibers and loosely packed, randomly oriented fibrils. Necrotic tissue typically appeared Ki-67-negative, often showed signs of tissue degradation, and was generally less cell dense. To facilitate comparison with the dMRI-based classification maps, digital images of the stained histological sections were processed using a supervised machine learning algorithm, which classified each pixel into one

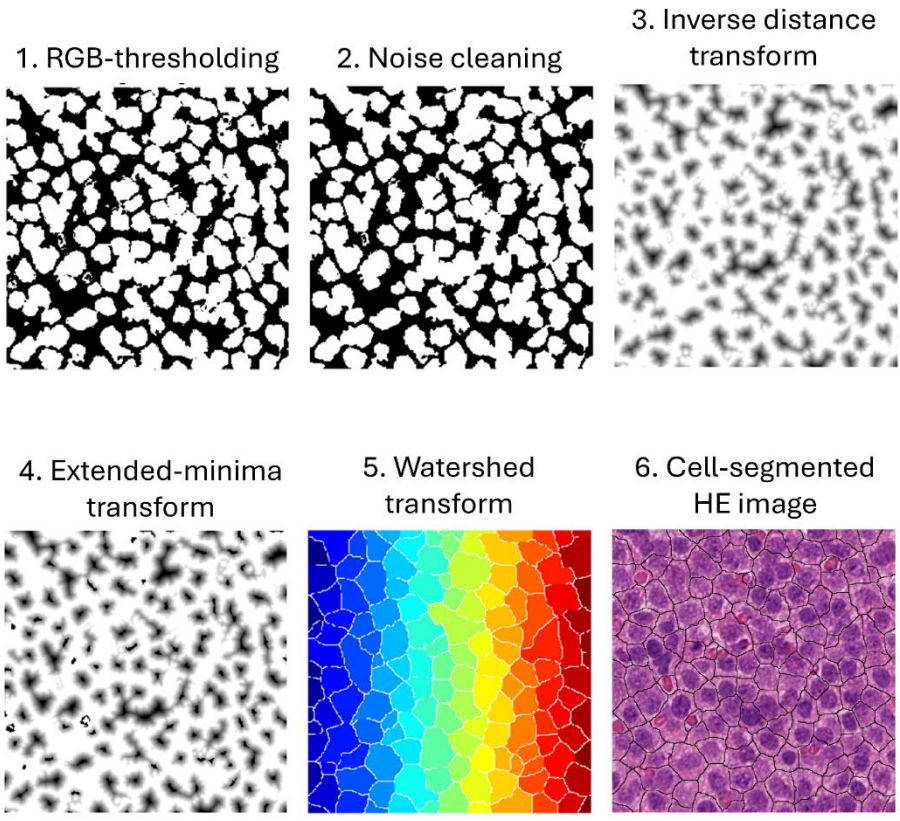

Figure 5. Example processing pipeline for segmenting cell nuclei from hematoxylin and eosin (HE) stained tumor tissue. RGB thresholding and noise removal provide an initial segmentation based on color intensities in the original HE image. Inverse distance mapping and extended-minima transformation are then applied to relate pixel values to their proximity to borders. Finally, a watershed algorithm performs the segmentation, typically resulting in one segmented object per cell nucleus

of the predefined tissue types. The algorithm was trained on manually labeled ROIs extracted from the tumor sections and subsequently applied to the full images to generate histology-based classification maps. An experienced morphologist reviewed and validated the output to ensure accurate labeling. Additionally, in Paper III, HE-stained sections were used to identify regions of high cell density within tumors, which were then used to assess the effects of

implementing a Monte Carlo (MC)-based model of EES diffusion. These regions were of particular interest, as the impact of the EES model was expected to be most pronounced in tissue with densely packed cells, i.e., where many barriers affect the EES diffusion.

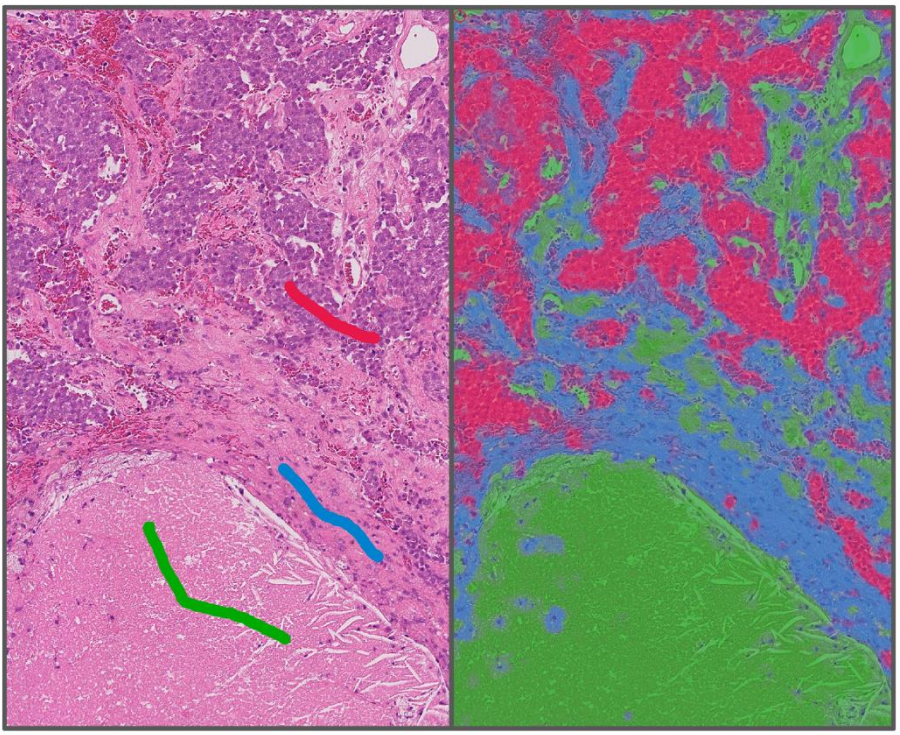

Figure 6. Example of tissue classification using supervised machine learning, shown here for a hematoxylin and eosin (HE) stained tumor tissue section. The algorithm is trained by manually labeling selected regions (left panel; color-coded annotations), in this case representing three distinct tissue classes (red, green, blue). Training is based on image features such as pixel intensity, edges, and textures, extracted using Gaussian filters at multiple scales to capture features at different levels of granularity. After training, the algorithm generates probability maps (right panel), where the color reflects the likelihood of each pixel to belong to a given class. The example shown was produced using minimal training data and limited optimization, and was implemented using the Ilastik software [78]

One major challenge, and a methodological limitation in Papers II and III, is the spatial registration between dMRI data and histological image data. Several factors make accurate alignment between these modalities difficult. First, a common feature or landmark must be present in both histological and MRI images to enable spatial alignment. In this thesis, tumors were marked with tissue ink at three points along the central transverse plane prior to full resection, corresponding to the plane of the central dMRI slice. The tumors were then sectioned such that the ink markings were visible in the histological sections, serving as anatomical reference points for registration. However, an important consideration is the discrepancy in slice thickness: histological sections are approximately 5 μm thick, whereas the dMRI slices are typically much thicker, 500 μm in Papers II and III. The histological sections therefore only represent a small subset of the dMRI slice. This also means that even when ink markings are visible in the histological sections, they may be angled differently relative to the dMRI image plane. As previously outlined, tissue morphology can change substantially between the *in vivo* dMRI acquisition and the *ex vivo* histological image, due to fixation, dehydration, and embedding. Additionally, MRI artifacts, especially spatial distortions caused by EPI-based readout, as commonly used in dMRI, also hinder accurate registration. To address these challenges, recent studies have explored, e.g., the use of 3D-printed molds to preserve tissue shape [9], as well as intermediate imaging techniques to better bridge MRI and histological data [79,80]. Despite these challenges, however, the dMRI data in Papers II and III showed good visual correspondence with histological data, but pixel-by-pixel registration between them was not feasible, preventing full quantitative comparison.

4.2 TREATMENT RESPONSE ASSESSMENT

Assessing treatment response is a critical component of the clinical cancer care workflow. Accurate assessment enables reevaluation of treatment strategies, helping to prevent both undertreatment and overtreatment. The standard clinical approach for evaluating response in solid tumors is based on volumetric measurements by comparing lesion size at baseline to follow-up time points, according to the widely used RECIST (Response Evaluation Criteria in Solid Tumors) guidelines [16]. However, changes in gross tumor volume can be delayed, while microstructural changes in the tissue occur earlier. For example, treatment-induced cell death may be preceded by changes in cell size [19,81–83]. Biophysical dMRI models, such as VERDICT, offer a promising method for detecting such microstructural changes, potentially

enabling earlier assessment of treatment response. The non-invasive nature of dMRI allows for repeated follow-up scans of the same tissue without affecting the biological environment, which is an advantage for longitudinal monitoring. In addition, VERDICT generates parameter maps that visualize the spatial heterogeneity of the tumor, offering more nuanced insight into how different tumor regions respond to therapy. This could ultimately support more tailored treatment adjustments, such as specifically targeting regions less likely to respond to the treatment. Figure 7 shows an example of VERDICT parameter maps over time following external radiation treatment in the GOT1 tumor model, illustrating the potential of this technique for spatiotemporal monitoring of treatment effects.

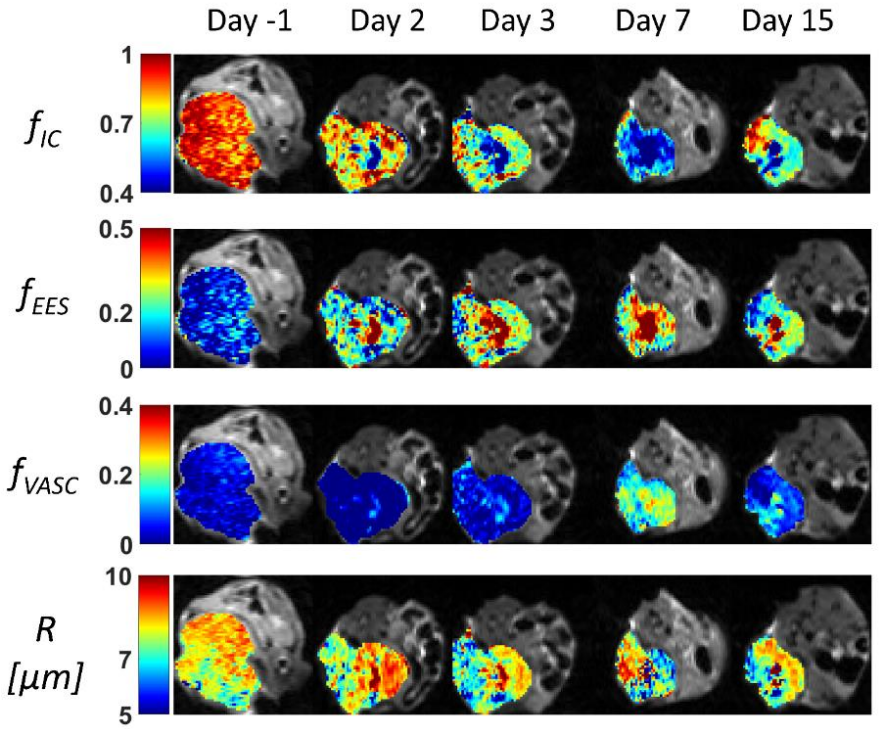

Figure 7. Color coded VERDICT parameter maps showing the central cross-section of a GOT1 tumor overlaid on a b=0 dMRI reference image of the mouse. Five repeated time points relative to the time point of external irradiation are shown for each parameter, enabling spatiotemporal monitoring of tumor tissue following treatment. Notable changes in parameter values are observed just a few days post-irradiation, both in the overall tumor-mean levels and in the spatial heterogeneity of the parameters

In Paper I, GOT1 tumors were externally irradiated and scanned using VERDICT MRI at baseline and at multiple follow-up time points, up to two weeks post-irradiation. Significant changes in several VERDICT parameters were observed within the first week after treatment. f_{IC} decreased, potentially reflecting reduced cell density due to cell death, while R increased, possibly indicating treatment-induced cell swelling. f_{VASC} displayed a delayed response, showing an increase on day 7, which may suggest increased perfusion following reduced cell density. These parameters were also evaluated against volume-based treatment response. Both f_{IC} and R demonstrated significant correlations with treatment response on days 3 and 6/7, respectively.

The VERDICT-derived parameters were also compared with those from other dMRI models and signal representations. When evaluating individual parameters, D_K, as derived from DKI, showed the strongest correlation with treatment response, while f_{IC} and ADC demonstrated only marginally weaker correlation. However, when parameters from each model were analyzed jointly using linear regression, the VERDICT model showed the highest explanatory value of treatment response, again on day 3. This finding reinforces the value of joint parameter analysis to fully leverage the information contained in the dMRI signal, connecting with the conclusions drawn in Paper II. It is important to note, however, that the VERDICT model was fitted to a more extensive set of dMRI acquisitions than the other models. Simpler representations such as ADC and DKI may not fully capture the information in the extensive signal dataset acquired with the VERDICT protocol, but it is possible that the improved explanatory value observed was a result of the richer acquisition scheme itself rather than the VERDICT model. Nevertheless, extracting meaningful information from such data likely requires a more complex model, such as VERDICT, that is better suited for fitting to the full signal data set.

Quantitative dMRI has been extensively studied for tumor treatment response assessment, with ADC being the most commonly used metric [84]. Although ADC is often interpreted to reflect cellularity, studies investigating this correlation have yielded inconsistent results, likely due to the complex and sometimes opposing ways in which tissue microstructure and biophysical properties influence ADC [85]. Biophysical models such as VERDICT, combined with dMRI protocols that vary diffusion time, offer parameter estimates that may help disentangle the underlying contributors to the dMRI signal. An additional advantage of such models is the improved interpretability of their parameters. While ADC is difficult to relate directly to specific tissue properties, VERDICT yields parameters with more direct biophysical

meaning, such as cell radius and intracellular volume fraction. However, caution must be taken when interpreting these parameters, as the VERDICT model represents a simplification of the true tissue microstructure.

In Paper II, VERDICT was evaluated for its ability to classify three distinct tumor tissue types in the GOT1 model: necrotic, fibrotic, and viable tumor tissue. Although histological analysis was only conducted at the final post-treatment time point (day 15) in Paper I, the observed VERDICT parameter changes at earlier time points can still be interpreted in the context of the classification results from Paper II. The observed reduction in f_{IC} during the first week post-irradiation suggests a shift from viable to non-viable tissue. Furthermore, both necrotic and fibrotic tissue exhibited low f_{IC} in Paper II, but were distinguishable by their R values, high in necrotic and low in fibrotic tissue, suggesting that the observed increase in R in Paper I may indicate the appearance of necrotic regions. However, because necrotic and fibrotic tissues showed opposing trends in R, their combined presence after treatment may result in little to no change in the tumor-mean R value, as was analyzed in Paper I. This highlights a potential limitation of using mean parameter values for treatment response evaluation. Using a clustering approach to monitor shifts in tissue composition (e.g., cluster fractions) across the tumor may reveal correlations with treatment response that are not captured by mean parameter analysis. Such an approach has demonstrated potential in previous studies using, e.g., clustering of dMRI and dynamic contrast enhanced (DCE) MRI data [86,87].

As previously noted, the use of VERDICT for diagnostic stratification has been explored in several studies. However, its application for treatment response assessment remains relatively underexplored. In an early study during the development of VERDICT, Panagiotaki et al. reported a significant decrease in f_{IC} and an increase in f_{VASC} following chemotherapy in a mouse model of colon adenocarcinoma [5]. These findings are consistent with the results presented in Paper I, although their study evaluated treatment effects at a much earlier time point, 5 hours post-treatment. Nonetheless, the results of Paper I demonstrate the potential of VERDICT for treatment response assessment and warrant further investigation in this area.

5 CONSIDERATIONS IN VERDICT MODELING

This chapter is mainly related to Papers III and IV.

In Paper III, the impact of diffusion time on the dMRI signal from the EES was investigated. A Monte Carlo-based model of EES diffusion was developed and incorporated into the VERDICT framework.

In Paper IV, the inclusion of compartment-specific T2 relaxation times in the VERDICT model and the use of different echo time schemes were evaluated for their impact on VERDICT parameter estimation.

The previous chapter outlined some potential applications of VERDICT, with findings from Papers I and II demonstrating its promise for non-invasive tumor tissue classification and early treatment response assessment. However, due to the large number of parameters in the model, it incorporates several simplifying assumptions about tissue microstructure and biophysical properties to ensure robust fitting. It is therefore essential to evaluate the impact of these assumptions and, where they introduce systematic errors, explore strategies to mitigate these or adapt the model to avoid relying on them.

Moreover, parameter estimates are only as informative as the underlying diffusion-weighted signal used for model fitting. Acquisition parameters, such as b-values and T_D, play an important role in determining parameter estimate accuracy and precision. Optimizing these parameters is particularly challenging in clinical settings, where scanner hardware capabilities are limited compared to preclinical systems. Many biophysical models, including VERDICT, were initially developed in preclinical settings with long scan times and high-performance gradients, enabling rich signal acquisition. Clinical translation, however, demands fast acquisition protocols that are compatible with clinical workflows while still providing adequate sensitivity to the underlying microstructure.

This chapter discusses some important considerations and limitations in VERDICT modeling.

5.1 COMPARTMENT-SPECIFIC RELAXATION

The fundamental concept of VERDICT modeling is that the MR signal originates from three distinct tissue compartments: intracellular (IC), vascular (VASC), and extracellular-extravascular space (EES). Each compartment is assumed to contribute with a distinct signal due to their unique microstructure and corresponding diffusion characteristics, allowing estimation of both compartmental volume fractions and compartment-specific microstructural parameters by fitting the model to the dMRI signal. VERDICT assumes that the only source of MR signal differences between compartments arises from differences in diffusion behavior. However, other phenomena can also substantially influence the MR signal, such as T1 and T2 relaxation, which are discussed in this chapter.

Briefly, T1 relaxation refers to the recovery of longitudinal magnetization following excitation, caused by energy transfer from excited spins to their surrounding environment. Because MRI involves repeated excitations that rotate longitudinal magnetization into the transverse plane for signal detection, T1 relaxation influences the MR signal intensity. The extent of this influence in dMRI is predominantly determined by the repetition time (TR). On the other hand, T2 relaxation relates to the dephasing of spins and subsequent decay of transverse magnetization due to spin-spin interactions, leading to signal decay over time after excitation. The influence of T2 relaxation on the MR signal is determined by the echo time (TE), which is the time between excitation and signal readout.

A key assumption in the classic VERDICT model is that T1 and T2 relaxation times are identical across all tissue compartments. When this assumption holds, relaxation effects are uniform and do not influence the relative signal contributions of each compartment, thereby not affecting parameter estimation – provided that a constant TE and TR are used across all acquisitions. However, if relaxation times differ between compartments, each compartment's signal will be differently weighted by relaxation-dependent scaling factors not accounted for in the model. Hence, a systematic error will be introduced in the estimated parameters. The impact of compartment-specific T1 relaxation can be mitigated by using a sufficiently long TR to reach nearly full longitudinal recovery in all compartments. However, mitigating the effects of compartment-specific T2 relaxation is more challenging, as it would require shortening the TE, which is inherently limited in dMRI sequences. The effect of compartment-specific T2 relaxation is unlikely to be negligible in

general, as several previous studies have demonstrated a dependence of dMRI-derived metrics on TE [21,88–91]. Figure 8 shows simulations illustrating the effect of compartment-specific T2 relaxation on the diffusion-weighted signal.

In a recent study by Palombo et al [44], an adapted version of VERDICT, called rVERDICT (relaxation-VERDICT), was suggested which accounts for relaxation as

$$S = S_{00}\left(1 - e^{-\frac{TR}{T1}}\right)\left[f_{VASC}e^{-\frac{TE}{T2_{VASC/EES}}}S_{VASC}(D_{VASC}, b) + f_{IC}e^{-\frac{TE}{T2_{IC}}}S_{IC}(D_{IC}, R, \delta, \Delta, G) + f_{EES}e^{-\frac{TE}{T2_{VASC/EES}}}S_{EES}(D_{EES}, b)\right] \quad (15)$$

where S_{00} is the signal at b = 0, TE = 0, and TR = ∞, and $T2_{\mathrm{VASC/EES}}$ and $T2_{\mathrm{IC}}$ are the T2 relaxation times of the VASC/EES and IC compartment, respectively. Note that the model does not consider compartment-specific T1 relaxation times and assumes that the T2 relaxation of the VASC and EES compartments are the same. The model was evaluated in patients with suspected prostate cancer and showed good agreement between T2 relaxation times estimated by rVERDICT and those obtained from independent multi-TE scans without diffusion weighting. For reference, the original version of the model, which does not include relaxation, will be referred to as classical VERDICT for the remainder of this chapter.

In Paper IV, a modified version of rVERDICT, excluding the T1 component of the model, was fitted to tumor data acquired in patients with intracranial brain tumors. In the dMRI protocol used, not only were diffusion-related sequence parameters varied, but also TE, and a dual-echo acquisition was used to acquire data with two TEs per scan. In previous studies, it has been a common strategy to use the minimum possible TE for each acquisition and fitting data to the signal normalized against S_0 [5]. Assuming the same T2 relaxation across compartments, this method will cancel out the effects of T2 relaxation on the signal. However, again, in the case of compartment-specific T2 relaxation, this method will introduce biases. In Paper IV, the dual-echo acquisition was set up so that the first echo was acquired with the minimum TE possible, and the second echo was acquired at a fixed TE of 140 ms. This

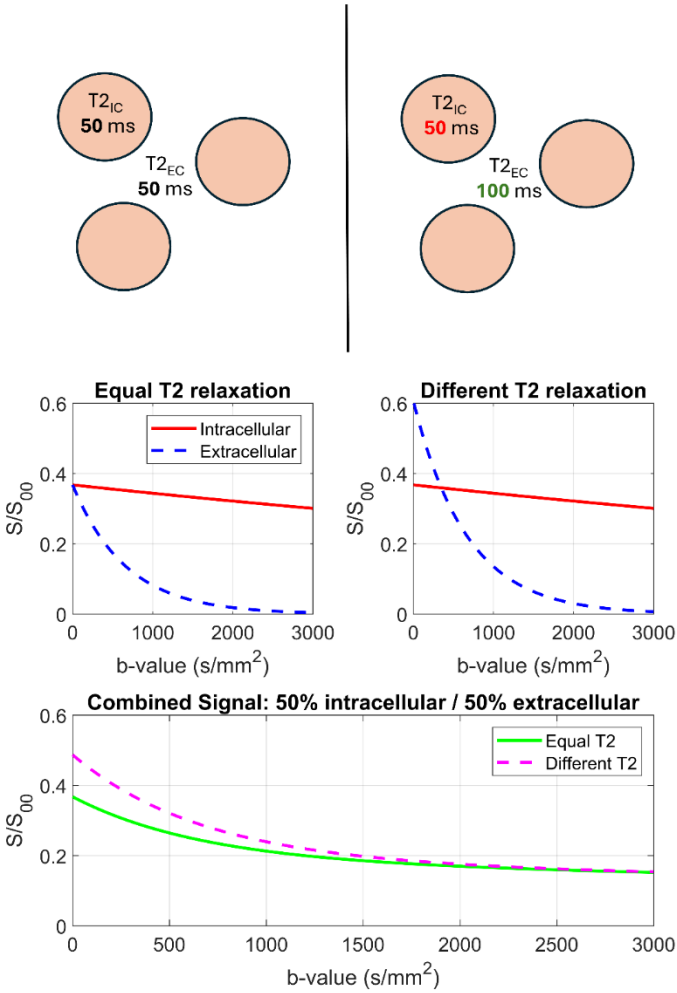

Figure 8. Simulations showcasing how differences in T2 relaxation times between intracellular (IC) and extracellular (EC) compartments can affect the total dMRI signal. In the left scenario, T2 relaxation times are equal across compartments, whereas in the right, the EC compartment exhibits a longer T2. The bottom panel shows the resulting total signal with the IC and EC contributions combined. In the case of different T2 relaxation, the EC signal dominates at low b-values due to slower T2 decay, leading to a steeper initial signal drop in the combined signal curve. Note that this behavior is specific for the simulated acquisition and microstructure parameters, and will vary under different conditions. Simulation parameters: TE = 50 ms, δ = 10 ms, Δ = 40 ms, $D_{IC} = D_{EC}$ = 1.5 µm²/ms, R = 5 µm

allowed for comparison of effects on classical VERDICT estimates when using either the minimum TE (S_{min}) or a fixed, longer TE (S_{140}), versus using data from both echoes in the fitting procedure with the rVERDICT model (S_{all}).

All VERDICT parameters estimated in Paper IV were significantly different when using S_{all} compared to S_{min} or S_{140}. For example, the mean f_{IC} across all included tumors was 0.56 for S_{all}, compared to 0.22 for S_{min} and 0.21 for S_{140}. $T2_{IC}$ was also estimated to be substantially lower (mean 62 ms) than the $T2_{VASC/EES}$ (mean 221 ms), indicating a much faster relaxation within the IC space. Assuming these estimates are accurate, not accounting for T2 relaxation – as in the classical VERDICT model – would result in a major impact on VERDICT parameter estimation in brain tumors. Given the notably shorter T2 relaxation time in the IC compartment, the corresponding signal at TEs commonly used in clinical settings (~60–100 ms) will be considerably lower than that of the other compartments. In classical VERDICT, where T2 relaxation differences are not modeled, this effect can only be accounted for by the diffusion-related parameters, leading to estimation bias. For instance, if the IC signal is disproportionately attenuated due to faster T2 relaxation decay relative to the other compartments, the model may compensate for the reduced signal contribution by underestimating f_{IC}.

This bias is relatively straightforward to understand when TE is constant across all measurements. However, when the minimum possible TE is used – resulting in TE varying across measurements – the situation becomes more complex. VERDICT can be viewed as a model that describes the diffusion-weighted MRI signal based on both biophysical tissue parameters and acquisition parameters. In order to estimate the biophysical parameters with good accuracy and precision, the acquired signals must sample a relevant proportion of the acquisition parameter space. In the case of rVERDICT, this space spans three key dimensions: b-value, T_D, and TE. Ideally, these parameters should be varied widely within a given protocol to maximize sensitivity to the underlying biophysical properties. However, the gradient separation time, Δ, plays a major role in constraining these parameters. Specifically, a low Δ is required to achieve short TE and T_D, while a high Δ is necessary for attaining high b-values, owing to hardware limitations on maximum gradient strength. In a clinical setting, this means that short TE and T_D can only be achieved at low b-values, as was the case in the acquisition protocol used in Paper IV. As a result, attempts to maximize the explored acquisition parameter space inherently introduce a positive correlation between b-value, T_D, and TE. The effects of introducing such parameter

correlations in the acquisition protocol are complex and depend heavily on the underlying microstructure and relaxation properties of the tissue, making them difficult to generalize and likely best explored through simulations. Nevertheless, one potential concern is that low T_D values are only explored at low b-values, which may limit sensitivity to fine-scale microstructural features. This is particularly important, as the signal is most sensitive to small-scale structures at short T_D and high b-values [92].

In a recent study by Jiang et al., a model similar to VERDICT – IMPULSED – was extended to include T2 relaxation effects and tested in a preclinical setting across multiple tumor models [21]. In three of the five tumor models, the authors reported a significantly shorter intracellular T2 relaxation time compared to the extracellular T2 relaxation time. A similar trend was observed for the two remaining tumor models, although it was not statistically significant. These findings are consistent with those presented in Paper IV, although the observed differences in T2 relaxation between compartments were less pronounced in the study by Jiang et al. Unlike the findings in Paper IV, Jiang et al. did not observe significant differences in most parameter estimates when including compartment-specific T2 relaxation and varying TE in the acquisition protocol. In the few cases where differences were significant, the changes in parameter estimates were minor. It is important to note that IMPULSED differs from VERDICT in several aspects. For example, it does not include a vascular compartment, and it incorporates both PGSE and OGSE acquisitions to access shorter T_D. Additionally, the impact of compartment-specific T2 relaxation is likely tissue-dependent, and the tumor models used in their study may not be representative of the tissue types investigated in Paper IV. Nevertheless, these somewhat conflicting results underscore the need for further investigation.

In general, including more free parameters, as is done in the rVERDICT model, leads to a more ill-posed fitting problem as the number of parameter combinations that can produce a plausible fit to the signal increases [93]. However, an important distinction in rVERDICT is the inclusion of varying additional acquisition parameters, namely TE and TR, which introduces new unique information in the signal. As a result, despite the additional free parameters, rVERDICT may remain comparably robust [94]. An alternative way of estimating compartment-specific T2 relaxation is to acquire a separate multi-TE scan without diffusion weighting and fit a multi-compartment relaxation model to the T2-weighted signal. However, there are two important considerations with this approach. First, clinical MRI protocols are often time-

constrained; as such, adding a separate T2-mapping sequence may not be feasible. In contrast, varying TE within the dMRI protocol and incorporating T2 relaxation directly into the model offers a more time-efficient way to expand the explored acquisition parameter space. Second, incorporating simultaneous sensitivity to both diffusion and relaxation in the signal may improve the ability to resolve individual parameters. For example, if two compartments differ in both their diffusion and relaxation properties, distinguishing them using signal data that varies both diffusion weighting and TE is likely more effective than analyzing each contrast separately [95]. If diffusion- and relaxation-related parameters are estimated from separate scans, they can still be jointly analyzed using, e.g., cluster analysis – a method which is investigated in Paper II. However, this approach only enables voxel-wise data clustering and does not aid in resolving information at the intra-voxel compartment level.

The results of Paper IV demonstrate that including compartment-specific T2 relaxation in the VERDICT model and varying TE in the acquisition protocol significantly impact parameter estimates in brain tumors. However, whether rVERDICT yields more accurate estimates than classical VERDICT cannot be concluded based on the limited data set in Paper IV. In one patient case involving resection of an astrocytoma, MR-guided biopsy samples were acquired and spatially linked to the corresponding VERDICT parameter maps, enabling comparison between model estimates and histological analysis. Two biopsy samples taken from distinct tumor regions were analyzed. The relative f_{IC} between the two locations showed good correspondence with histology: the tissue sample with higher cell density exhibited nearly double the f_{IC} value compared to the sample with lower cell density. However, this relative difference was consistent across all fitting scenarios S_{all}, S_{min}, and S_{140}, and thus does not establish which scenario provided the most accurate f_{IC} estimate. The histological evaluation was conducted using HE staining, which, as previously described, provides excellent contrast for general tissue morphology. However, HE staining does not clearly delineate cell membranes; only cell nuclei are stained prominently by hematoxylin. Therefore, to quantify and validate specific tissue features that are more directly related to VERDICT parameters – such as f_{IC} and R – additional staining methods would be required.

5.2 DIFFUSION TIME-DEPENDENCE

To separate the signal contributions of different compartments, VERDICT relies on differences in the motion of water molecules within each compartment. The VASC compartment is distinguishable due to the presence of flow, which causes a fast signal decay with increasing b-values. In contrast, motion-related signal attenuation in the IC and EES compartments is driven solely by diffusion, resulting in a more gradual decay with increasing b-value. In both the IC and EES compartments, cell membranes will act as barriers that influence diffusion behavior. A key distinction between these two compartments, commonly used in biophysical dMRI modeling, is that diffusion in the IC compartment is considered *restricted*, while diffusion in the EES is considered *hindered* [96]. Restricted diffusion refers to the scenario where water molecules are confined within closed spaces, such as the IC space, meaning they cannot move beyond the enclosed barriers regardless of diffusion time, T_D. In contrast, hindered diffusion refers to the scenario where barriers are present but do not fully enclose the water molecules, allowing them to move increasingly farther with increasing T_D. This distinction is particularly important, as many biophysical dMRI models, including VERDICT, utilize the different signal behaviors of restricted and hindered diffusion across varying T_D to disentangle the contributions of the IC and EES compartments.

VERDICT models the diffusion-weighted signal from the EES compartment according to Equation (10) as presented in Chapter 3.3. A key observation is that the EES signal model depends solely on the b-value among acquisition parameters, while the IC model depends explicitly on the diffusion gradient timing parameters, Δ and δ. Importantly, the same b-value can be achieved using different combinations of these timing parameters by varying the gradient strength, as can be realized when inspecting Equation (2). In other words, the EES signal is considered diffusion time-independent, whereas the IC signal is considered diffusion time-dependent. To understand the rationale for modeling the EES compartment as time-independent, it is helpful to consider the theoretical limits of T_D. At very short T_D, often referred to as the short-time regime, water molecules generally do not travel far enough for the diffusion-weighted signal to reflect the presence of true geometric restrictions [97]. However, barriers still influence diffusion in this regime, as molecules located near them at the start of the diffusion sensitization have time to interact with them. With increasing T_D, more molecules will interact with the barriers, leading to a diffusion time-dependence. In the short-time regime, the diffusivity depends on the surface-to-volume ratio of the microstructure, which

describes the amount of barrier surface area per unit volume [98]. For typical *in vivo* microstructures, reaching this regime is not feasible with PGSE but can be achieved using OGSE [99]. At the other extreme, very long T_D values define what is referred to as the tortuosity limit, where sufficient coarse-graining has occurred such that the signal becomes insensitive to fine structural features [97]. In this context, coarse-graining refers to diffusion occurring over a timescale long enough to effectively average over smaller structural details. In this regime, diffusion is considered Gaussian and no longer diffusion time-dependent. A particularly interesting case to consider is restricted diffusion at the tortuosity limit. In this case, since spins are confined within a finite space, the diffusion sensitization becomes limited, and the effective diffusion coefficient will converge towards $D_{eff} = 0$ with increasing T_D. Figure 2 in Chapter 3.4 illustrates diffusion behavior in the EES compartment for different time regimes.

An important observation is that diffusion in the EES transitions from being time-dependent in the short-time regime to time-independent at the tortuosity limit. The signal behavior between these two extremes is much more difficult to describe analytically. However, Novikov et al. have demonstrated that, for systems with structural barriers, D_{eff} decreases with T_D according to a power law, converging toward some tortuosity limit diffusion coefficient, D_∞ [37]. The VERDICT model assumes that T_D is sufficiently long for the EES diffusion to have reached the tortuosity limit, where diffusion can be approximated as Gaussian and diffusion time-independent [97]. However, it is not clear that this assumption holds for the diffusion times and tissue microstructures typically explored in VERDICT applications. While the diffusion-weighted signal from restricted diffusion in well-defined, simple geometries – such as spheres – has been derived analytically [35], modeling the EES is more challenging due to its complex barrier configuration. As an alternative, Monte Carlo (MC) simulations can be used to study hindered diffusion in geometries that resemble the structural complexity of the EES [24].

Two important parameters are defined here for reference throughout the remainder of this chapter. First, the intrinsic diffusion coefficient, D_{int}, refers to the diffusion coefficient in the absence of barriers. It can be thought of as the free or unrestricted diffusion coefficient. In the context of simulations, D_{int} can still be defined even when barriers are present, representing the diffusivity that the water molecules would exhibit if no barriers existed. Second, the bulk diffusion coefficient, D_{bulk}, describes the effective diffusion coefficient when

both the intrinsic diffusivity and the influence of barriers are taken into account. As a consequence, D_{bulk} is always lower or equal to D_{int}.

In Paper III, MC simulations were used to study the EES signal using a PGSE sequence with diffusion times typical of VERDICT protocols (Δ = 10–40 ms, δ = 5 ms). A digital 3D mesh composed of packed spheres was generated to mimic a simplified EES geometry, within which the simulations were conducted. To explore different microstructural configurations, multiple meshes were created by varying the cell radius (R) from 5 to 15 μm and the intracellular volume fraction (f_{IC}) from 0.1 to 0.9. Simulations were also performed across a range of D_{int} from 1 to 3 μm^2/ms to represent different intrinsic EES diffusivity scenarios. All random walkers were initialized in the EES, and cell membranes were modeled as impermeable, such that no inter-compartmental exchange occurred.

For simulation geometries with $f_{IC} < 0.8$, Paper III showed effectively no diffusion time-dependence in the EES signal. In these cases, the signal could be well described using a diffusion time-independent Gaussian model, consistent with the tortuosity-limit assumption made in VERDICT. However, for higher cell-packing densities, particularly at $f_{IC} \geq 0.9$, a distinct diffusion time dependence was observed, indicating that the tortuosity limit had not yet been reached within the studied T_D range. These results suggest that the tortuosity-limit assumption in the EES may not hold in tumor tissue with high cell density. In previous VERDICT studies on prostate and brain tumors, estimated f_{IC} values have typically remained below the threshold where this effect would become relevant [7,43]. However, a recent study by Wang et al. reported estimated extracellular volume fractions (f_{EC}) in breast tumor tissue of 20.4 ± 8.2% (mean ± SD) using dual-energy CT, corresponding to f_{IC} values in the range of approximately 0.7 to 0.9 [100]. Histological analysis of two breast cancer subtypes in the same study yielded f_{EC} values of 6.1% and 30.2%. Panagiotaki et al. also reported a mean f_{IC} of 0.84 in a tumor model of colorectal adenocarcinoma [5]. Additionally, in Papers I and II, f_{IC} estimates exceeded 0.8 in a notable number of voxels within the GOT1 tumor model (a small-intestine neuroendocrine tumor model), reinforcing the idea that VERDICT's tortuosity-limit assumption in the EES may not universally apply across all tumor types. Moreover, as discussed in the previous chapter, not accounting for compartment-specific T2 relaxation may introduce additional bias in f_{IC} estimations. In Paper IV, fitting scenarios that did not include compartment-specific T2 relaxation yielded mean f_{IC} values of 0.21 and 0.22 in brain tumors, whereas including compartment-specific T2 relaxation raised the mean to 0.56,

with one of the tumors, a meningioma, reaching a tumor mean f_{IC} above 0.8. As such, in previous studies using classical VERDICT, this T2-related bias may have led to a systematic underestimation of f_{IC}.

An interesting observation in Paper III was seen when analyzing the simulated EES signal: for simulation meshes with smaller cell sizes (R = 5 μm), D_{bulk} increased with increasing T_D, while for larger cell sizes (R = 15 μm), D_{bulk} decreased with T_D. A recent study by Xu et al. investigated diffusion time dependence in the EES using finite difference simulations in a heterogeneous mesh with varying cell radii [23]. In contrast to the findings in Paper III, they reported a monotonic decrease in D_{bulk} with increasing T_D, both in simulations and in a physical phantom composed of liposomes filled with deuterium oxide and suspended in water. The increase in D_{bulk} with T_D observed in Paper III for small R may be tied to the specific geometry of the simulation mesh used. In Paper III spheres were packed in a face-centered cubic arrangement, which allows for a maximum f_{IC} of 0.74 before overlap occurs. To simulate higher f_{IC} values, the spheres were allowed to overlap, although random walkers were still initialized in the fully extracellular space. This led to a characteristic mesh geometry in which the extracellular pathways between cells became narrower as f_{IC} increased. Importantly, even at the highest simulated packing (f_{IC} = 0.9), the walkers were not fully confined, i.e. diffusion was hindered rather than restricted.

This EES signal behavior seen in Paper III can be interpreted in the context of the diffusion time regimes discussed earlier in this chapter. For larger R, the intercellular distances are larger relative to the effective diffusion length (L_D), making the system more closely resemble the short-time regime. In this regime, increasing T_D leads to more interactions with barriers and thus a decrease in D_{bulk}. For smaller R, however, the intercellular distances are smaller relative to L_D and the walkers have time to explore more of the geometry. Due to the narrow pathways between cells, the diffusion may here resemble a pseudo-restricted regime, and as T_D increases, walkers eventually navigate through these narrow pathways, accessing larger regions of space. This can be viewed as a transition from a short-time regime, to a pseudo-restricted intermediate-time regime, and eventually toward a hindered long-time regime. Importantly, this specific signal behavior may be a consequence of the highly symmetrical geometry used in the simulations. In a more realistic tissue configuration with heterogeneous cell sizes and densities within a voxel, such effects may average out, resulting in a voxel-level signal that shows a monotonic decrease in D_{bulk} with increasing T_D, as reported by Xu et al [23].

Due to the complexity of analytically modeling EES diffusion outside the well-defined diffusion time regimes, Paper III investigated an alternative approach using an MC-based EES model. Regardless of whether least squares, dictionary-based, or deep neural network (DNN) fitting strategies are used, the underlying principle of model fitting involves exploring model output across a range of parameter combinations. This output can then be used to, e.g., minimize fitting errors, construct a signal dictionary, or train a predictive model. In Paper III, MC simulations were used to generate diffusion-weighted signal values for a range of EES conditions, with both geometry- and diffusivity-related simulation parameters varied. The resulting dataset could then be used for model fitting to measured signal values. However, a key limitation of MC simulations is the high computational cost, which restricts the number of parameter combinations that can be practically simulated. To address this, Paper III limited the resolution of the simulation parameter grid and applied a cubic spline interpolation to create a continuous signal model. The interpolation yielded a piecewise cubic function with smooth transitions between sampled parameter points, allowing for rapid analytical signal generation across the entire parameter space. The MC-based model was evaluated *in vivo,* in GOT1 tumors, by replacing the Gaussian EES compartment in VERDICT with the interpolated MC-based model. Histological image data, spatially matched with dMRI images, was used to ensure that the model was evaluated in regions of high cell density. Most VERDICT parameter estimates showed statistically significant differences between the Gaussian and MC-based EES models, although the absolute differences were modest. For example, f_{IC} was estimated to be lower with the MC-based model. This may be due to the Gaussian model's assumption of time-independent diffusion in the EES; as a result, any observed diffusion time-dependence in the signal may be mistakenly attributed to the IC compartment, leading to an overestimation of f_{IC}.

Although the MC-based model used in Paper III accounts for diffusion time dependence in the EES compartment, it still relies on simplifying assumptions, particularly regarding the geometry of EES barriers. The model assumes that cells within the voxel are of equal size and spaced equidistantly. These assumptions may introduce other forms of bias, as they do not reflect the inherent heterogeneity of real tissue. Incorporating parameters that relate to heterogeneity, such as variance in cell radius, could potentially make the model more realistic but would also increase model complexity and reduce robustness, making parameter estimation more unstable. Furthermore, adding heterogeneity to the simulation mesh would require a sufficiently large

simulation volume to ensure the resulting signal is statistically representative [101]. Despite these limitations, Monte Carlo-based modeling remains a promising approach for microstructural characterization, and similar methods have previously shown potential in brain tissue fingerprinting [102,103].

6 CONCLUSION

This thesis investigated the use of VERDICT for applications in tumor tissue characterization and response assessment, as well as the impact of modeling assumptions on parameter estimates. The work included studies on a mouse model of small-intestine neuroendocrine tumor (GOT1; Papers I, II, and III) and human brain tumors (Paper IV). Specifically, it was shown that:

- analyzing dMRI data using VERDICT modeling has potential for early assessment of radiation treatment response. When parameters are analyzed jointly using linear regression, VERDICT provides higher explanatory value for treatment response compared to ADC, IVIM, or DKI (Paper I)

- clustering of the VERDICT parameters R and f_{IC} using Gaussian mixture modeling enables classification of tumor voxels into viable, necrotic, and fibrotic tissue (Paper II)

- disregarding diffusion time-dependence in the extracellular-extravascular space (EES) introduces estimation biases in tumor tissue with high cell density, although of relatively small magnitude. A method combining Monte Carlo-based modeling of the EES diffusion and a learning-based parameter estimation approach was developed, and shows promise in mitigating these biases (Paper III)

- model assumptions related to compartment-specific T2 relaxation in brain tumors strongly influence VERDICT parameter estimates. When compartment-specific T2 relaxation is excluded in the model, parameter estimates vary with the choice of TE. A multi-TE dMRI acquisition was developed and combined with relaxation-VERDICT analysis, and shows promise in mitigating these effects (Paper IV)

Overall, this thesis demonstrates that VERDICT is a promising non-invasive method for whole-tumor tissue characterization and treatment assessment. The thesis also presents methodological developments and implementations aimed at mitigating parameter estimation biases in VERDICT modeling.

7 FUTURE PERSPECTIVES

Biophysical dMRI modeling, such as VERDICT, holds great potential for non-invasive characterization of tissue microstructure, with spatially resolved information across entire volumes of interest. These methods have broad potential for both research and clinical applications, as reflected by the substantial increase in publications on microstructural imaging with dMRI since the early 2000s and the sustained interest over the past years (Figure 9). However, dMRI modeling remains an inverse and often ill-posed problem, where multiple microstructural arrangements can produce similar diffusion signals [104]. Model complexity, coupled with sensitivity to noise, often necessitates regularization, parameter constraints, or simplifying assumptions to achieve stable parameter estimation. Despite decades of research, clinical translation has been slow, underscoring the challenges in bringing these models, including VERDICT, into routine clinical practice [4]. Addressing these challenges will be crucial for advancing the field and realizing the clinical potential of biophysical dMRI modeling [105].

One of the fundamental challenges in the clinical translation of VERDICT is the limited hardware performance of clinical MRI scanners compared to those used in pre-clinical research. High gradient strengths are often required to achieve the high b-values and short diffusion times necessary for sensitivity to fine-scale microstructural features [106]. However, clinical MRI systems typically offer lower gradient performance, and scan times are tightly constrained within standard clinical workflows. These factors limit both the achievable acquisition parameter space and the signal-to-noise ratio (SNR). While hardware capabilities are gradually improving [107,108], progress can also be made through protocol optimization. This includes identifying acquisition parameter combinations that yield the most informative signal data for accurate parameter estimation. Because model-derived parameters may vary depending on acquisition parameters, protocol standardization across imaging sites may also become necessary. Moreover, larger-scale multi-site reproducibility studies will be important to ensure generalizability and clinical reliability.

VERDICT is a relatively complex model, yet it still relies on several simplifying assumptions. As investigated in this thesis, assumptions such as homogeneous T2 relaxation times across compartments and Gaussian, time-independent diffusion in the EES can introduce biases that substantially

influence parameter estimates. Other potential sources of bias warrant further investigation – for example, water exchange between compartments, driven by permeability across capillary walls and cell membranes [109]. The model also assumes spherical cell geometry and estimates only a single parameter to describe cell radius. However, tumor tissue often exhibits deviations from spherical cell shapes and contains a heterogeneous distribution of cell sizes within a voxel. These structural complexities may affect parameter accuracy and should be explored in future work. Ultimately, there is a necessary trade-off between model complexity and estimation robustness. Incorporating too many biophysical parameters can lead to instability and unreliable estimates. An alternative strategy is to simplify the model through careful selection of acquisition parameters that suppress or minimize the influence of specific effects. For example, excluding low b-values (< 200 s/mm²) can reduce signal contributions from perfusion [2,110], while using short diffusion times may help avoid confounding effects of inter-compartmental exchange [111]. These acquisition-based strategies represent a promising direction and warrant further investigation in future studies.

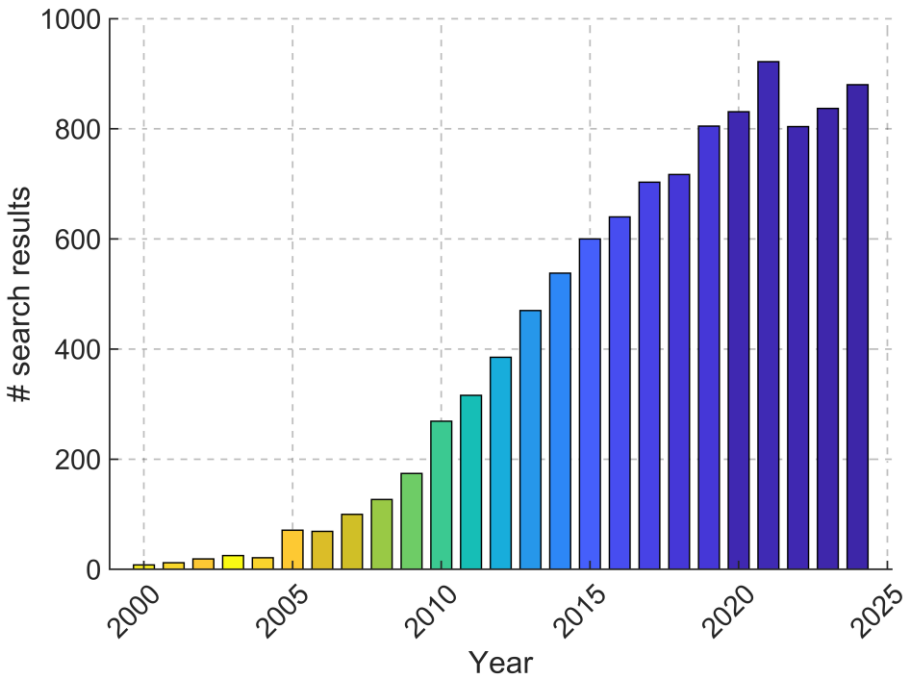

Figure 9. Number of PubMed search results by year of publication (2000 to 2024) using the search string: 'MRI' AND 'diffusion' AND 'microstructure'

Another potential avenue for improving VERDICT model robustness is the use of novel model-fitting approaches. Among these, both trained supervised and self-supervised DNNs have shown promise for estimating VERDICT parameters directly from diffusion MRI signals [44,112]. By including realistic noise in the training data, DNNs can learn to produce more stable parameter estimates even in lower SNR conditions. Once trained, DNNs enable rapid parameter estimation, making this approach particularly attractive for time-constrained clinical workflows. Moreover, DNNs are capable of learning complex, non-obvious dependencies between signal features and model parameters, which may result in more accurate and stable estimates compared to conventional fitting methods. However, DNNs are still sensitive to bias introduced by inaccuracies in the forward model, and, in the case of supervised training, their performance is highly dependent on the quality and representativeness of the training data. Effective DNN training also requires careful tuning of hyperparameters such as regularization strategies and network architecture. As such, there is considerable potential for further development and optimization of DNN-based model fitting for VERDICT.

The ultimate goal of biophysical dMRI modeling is to non-invasively and accurately measure the microstructure and biophysical processes of living tissue. However, due to the complexity and heterogeneity of real biological tissue, this dream may never be fully realized. Nonetheless, validation remains a critical step in assessing model reliability and refining their practical value. This validation can occur across multiple stages, from concept to clinical application. Numerical simulations using synthetic phantoms offer controlled environments with known ground truths, providing a foundation for initial evaluation of model performance, sensitivity, and limitations [24]. Examples of recent developments in this field include advancements in simulating permeable layers [113] and numerical phantoms generated by mimicking biological growth processes [114]. Physical phantoms serve as an important bridge between simulation and *in vivo* studies, enabling validation under real experimental conditions while still maintaining access to known ground-truth values. Constructing physical phantoms that accurately represent specific aspects of biological tissue is a challenging task that often demands considerable creativity. Recent approaches have included the use of liposome-based phantoms to mimic densely packed cellular environments [23], as well as 3D-printed structures designed to replicate axonal fiber bundles in white matter [115]. Finally, *in vivo* validation, through comparison with, e.g., histological or electron microscopy data, is essential to align model-derived parameters with actual tissue microstructure. Continued development in all

these areas will be crucial for advancing biophysical modeling approaches such as VERDICT, and for making them robust and reliable enough to provide meaningful value in clinical practice.

ACKNOWLEDGEMENT

A PhD student's journey is filled with adventure, exploration, challenges, and countless lessons learned. I have been fortunate to be surrounded by many wonderful people along the way. To all of you, I wish to extend my deepest gratitude.

Maria Ljungberg, supervisor. You have been an anchor, a rock to lean on, and a lighthouse guiding me through the sometimes confusing world of research. You encouraged me to explore my ideas, while also helping me stay focused on the bigger picture. I truly couldn't have asked for a better supervisor.

Mikael Montelius, co-supervisor. You gave the very first lecture I ever attended on MR physics, and from that moment, I knew I wanted to dive deeper into this fascinating world of spins and magnetic fields. Since then, we've shared many laughs and "Eureka!" moments in the lab. Your curious and creative mind has been a constant reminder that research can, and should, be fun!

Oscar Jalnefjord, co-supervisor. When it comes to bouncing ideas and hypotheses in MR physics, I don't think anyone in the world is more suited for the task. You always had the answers to my questions, even though I somehow would leave our conversations with ten new ones! You have kept my mind active, challenged my ideas, and helped me discover new paths to explore.

Eva Forssell-Aronsson, co-supervisor. If I looked up "Radiophysics" in the dictionary, I'm pretty sure your name would be right there. Your vast experience helped me make sense of academia when I was confused, and you showed me the value of tradition and the work of those who came before us.

My PhD student office roommates over the years, **Jens**, **Emilia**, **Frida**, **Louise**, **Alma**, and **Elina**. I could write an entire thesis on the good times we've shared. From climbing adventures and pub nights to late evenings trying to shave ten more words off the abstract. Rest assured, my memories with you are full of laughter and appreciation.

All the rest of the PhD students at the Department of Medical Radiation Sciences. Together, we've shared the peculiar struggles of a PhD student's life, and I'm grateful to have shared them with you!

The MR physics group, clinicians, researchers, and lecturers at the Department of Medical Radiation Sciences. The Sahlgrenska Academy is a fantastic place to pursue a PhD, but it's the people who truly make it special. Thank you for making it such a welcoming, inspiring, and collaborative environment.

To my family. Your endless love and support have helped me believe in myself. Perhaps now, I've finally caught up with my childhood idol – Balthazar!

The work presented in this thesis was supported by grants from the Swedish Cancer Society, the Swedish Research Council, the King Gustav V Jubilee Clinic Cancer Research Foundation, BioCARE – a National Strategic Research Program at the University of Gothenburg, the Swedish state under the agreement between the Swedish government and the county councils, the ALF agreement, the Sahlgrenska University Hospital Research Funds, the Assar Gabrielsson Cancer Research Foundation, the Adlerbertska Research Foundation, the Herbert & Karin Jacobsson Foundation, the Royal Society of Arts and Sciences in Gothenburg (KVVS), Lion's Cancer Research Fund of Western Sweden, and the Wilhelm and Martina Lundgren Research Foundation.

STATEMENT ON THE USE OF GENERATIVE AI

The OpenAI ChatGTP 4o model was used during the writing process of this thesis frame to improve readability. Specifically, the model was employed as aid in copy editing during revision of the text. When deployed, the model's input consisted of individual sentences to revise and a prompt requesting suggested edits to improve grammar and clarity. The model's output was carefully reviewed and, when used, revised and edited to ensure that the message and nuance of the original text were unaltered. Additionally, the "opt-out" option to not share data for further model training was selected. The author takes full responsibility for the content of this thesis frame.

REFERENCES

1. Stejskal EO, Tanner JE. Spin Diffusion Measurements: Spin Echoes in the Presence of a Time-Dependent Field Gradient. J Chem Phys. 1965;42(1):288-292. doi:10.1063/1.1695690
2. Le Bihan D, Breton E, Lallemand D, Grenier P, Cabanis E, Laval-Jeantet M. MR imaging of intravoxel incoherent motions: application to diffusion and perfusion in neurologic disorders. Radiology. 1986;161(2):401-407. doi:10.1148/radiology.161.2.3763909
3. Einstein A. Über die von der molekularkinetischen Theorie der Wärme geforderte Bewegung von in ruhenden Flüssigkeiten suspendierten Teilchen. Ann Phys. 1905;322(8):549-560. doi:10.1002/andp.19053220806
4. Novikov DS, Kiselev VG, Jespersen SN. On modeling. Magn Reson Med. 2018;79(6):3172-3193. doi:10.1002/mrm.27101
5. Panagiotaki E, Walker-Samuel S, Siow B, et al. Noninvasive quantification of solid tumor microstructure using VERDICT MRI. Cancer Res. 2014;74(7):1902-1912. doi:10.1158/0008-5472.CAN-13-2511
6. Singh S, Rogers H, Kanber B, et al. Avoiding Unnecessary Biopsy after Multiparametric Prostate MRI with VERDICT Analysis: The INNOVATE Study. Radiology. Published online 2022. doi:10.1148/radiol.212536
7. Zaccagna F, Riemer F, Priest AN, et al. Non-invasive assessment of glioma microstructure using VERDICT MRI: correlation with histology. Eur Radiol. Published online March 19, 2019:1-8. doi:10.1007/s00330-019-6011-8
8. Lundholm L, Montelius M, Jalnefjord O, Forssell-Aronsson E, Ljungberg M. VERDICT MRI for radiation treatment response assessment in neuroendocrine tumors. NMR Biomed. 2022;35(6):1-14. doi:10.1002/nbm.4680
9. Bailey C, Bourne RM, Siow B, et al. VERDICT MRI validation in fresh and fixed prostate specimens using patient-specific moulds for histological and MR alignment. NMR Biomed. 2019;32(5):e4073. doi:10.1002/nbm.4073

10. Louis DN, Perry A, Wesseling P, et al. The 2021 WHO Classification of Tumors of the Central Nervous System: a summary. Neuro Oncol. 2021;23(8):1231-1251. doi:10.1093/neuonc/noab106

11. Netto GJ, Amin MB, Berney DM, et al. The 2022 World Health Organization Classification of Tumors of the Urinary System and Male Genital Organs—Part B: Prostate and Urinary Tract Tumors. Eur Urol. 2022;82(5):469-482. doi:10.1016/j.eururo.2022.07.002

12. Avcı S, Öner S, Önen E, Çağlayan V, Kılıç M, Şambel M. Risk Factors Affecting Complications Due to Prostate Biopsy. The Bulletin of Urooncology. 2019;18(2):46-50. doi:10.4274/uob.galenos.2018.1149

13. Malone H, Yang J, Hershman DL, Wright JD, Bruce JN, Neugut AI. Complications Following Stereotactic Needle Biopsy of Intracranial Tumors. World Neurosurg. 2015;84(4):1084-1089. doi:10.1016/j.wneu.2015.05.025

14. Carano RAD, Ross AL, Ross J, et al. Quantification of Tumor Tissue Populations by Multispectral Analysis. Magn Reson Med. 2004;51(3):542-551. doi:10.1002/mrm.10731

15. Jalnefjord O, Montelius M, Arvidsson J, Forssell-Aronsson E, Starck G, Ljungberg M. Data-driven identification of tumor subregions based on intravoxel incoherent motion reveals association with proliferative activity. Magn Reson Med. 2019;82(4):1480-1490. doi:10.1002/mrm.27820

16. Eisenhauer EA, Therasse P, Bogaerts J, et al. New response evaluation criteria in solid tumours: revised RECIST guideline (version 1.1). Eur J Cancer. 2009;45(2):228-247. doi:10.1016/j.ejca.2008.10.026

17. Verma N, Cowperthwaite MC, Burnett MG, Markey MK. Differentiating tumor recurrence from treatment necrosis: a review of neuro-oncologic imaging strategies. Neuro Oncol. 2013;15(5):515-534. doi:10.1093/neuonc/nos307

18. Young RJ, Gupta A, Shah AD, et al. Potential utility of conventional MRI signs in diagnosing pseudoprogression in glioblastoma. Neurology. 2011;76(22):1918-1924. doi:10.1212/WNL.0b013e31821d74e7

19. Bortner CD, Cidlowski JA. A necessary role for cell shrinkage in apoptosis. Biochem Pharmacol. 1998;56(12):1549-1559. doi:10.1016/s0006-2952(98)00225-1

20. Jelescu IO, Veraart J, Fieremans E, Novikov DS. Degeneracy in model parameter estimation for multi-compartmental diffusion in neuronal tissue. NMR Biomed. 2016;29(1):33-47. doi:10.1002/nbm.3450

21. Jiang X, Harkins KD, Xie J, et al. Joint estimation of compartment-specific T2 relaxation and tumor microstructure using multi-TE IMPULSED MRI. Magn Reson Med. 2025;93(1):96-107. doi:10.1002/mrm.30254

22. Reynaud O. Time-Dependent Diffusion MRI in Cancer: Tissue Modeling and Applications. Front Phys. 2017;5:58. doi:10.3389/fphy.2017.00058

23. Xu J, Xie J, Semmineh NB, Devan SP, Jiang X, Gore JC. Diffusion time dependency of extracellular diffusion. Magn Reson Med. 2023;89(6):2432-2440. doi:10.1002/mrm.29594

24. Fieremans E, Lee HH. Physical and numerical phantoms for the validation of brain microstructural MRI: A cookbook. Neuroimage. 2018;182:39-61. doi:10.1016/j.neuroimage.2018.06.046

25. Stejskal EO, Tanner JE. Spin diffusion measurements: Spin echoes in the presence of a time-dependent field gradient. J Chem Phys. 1965;42(1):288-292. doi:10.1063/1.1695690

26. Jensen JH, Helpern JA, Ramani A, Lu H, Kaczynski K. Diffusional kurtosis imaging: the quantification of non-gaussian water diffusion by means of magnetic resonance imaging. Magn Reson Med. 2005;53(6):1432-1440. doi:10.1002/mrm.20508

27. Zhang H, Schneider T, Wheeler-Kingshott CA, Alexander DC. NODDI: Practical in vivo neurite orientation dispersion and density imaging of the human brain. Neuroimage. 2012;61(4):1000-1016. doi:10.1016/j.neuroimage.2012.03.072

28. le Bihan D, Breton E, Lallemand D, Aubin ML, Vignaud J, Laval-Jeantet M. Separation of diffusion and perfusion in intravoxel incoherent motion MR imaging. Radiology. 1988;168(2):497-505. doi:10.1148/radiology.168.2.3393671

29. Jiang X, Li H, Xie J, Zhao P, Gore JC, Xu J. Quantification of cell size using temporal diffusion spectroscopy. Magn Reson Med. 2016;75(3):1076-1085. doi:10.1002/mrm.25684

30. Federau C. Intravoxel incoherent motion MRI as a means to measure in vivo perfusion: A review of the evidence. NMR Biomed. 2017;30(11):1-15. doi:10.1002/nbm.3780

31. Ahlgren A, Knutsson L, Wirestam R, et al. Quantification of microcirculatory parameters by joint analysis of flow-compensated and non-flow-compensated intravoxel incoherent motion (IVIM) data. NMR Biomed. 2016;29(5):640-649. doi:10.1002/nbm.3505

32. Panagiotaki E, Schneider T, Siow B, Hall MG, Lythgoe MF, Alexander DC. Compartment models of the diffusion MR signal in brain white matter: A taxonomy and comparison. Neuroimage. 2012;59(3):2241-2254. doi:10.1016/j.neuroimage.2011.09.081

33. Wu D, Zhang J. Evidence of the diffusion time dependence of intravoxel incoherent motion in the brain. Magn Reson Med. 2019;82(6):2225-2235. doi:10.1002/mrm.27879

34. Murday JS, Cotts RM. Self-diffusion coefficient of liquid lithium. J Chem Phys. 1968;48(11):4938-4945. doi:10.1063/1.1668160

35. Neuman CH. Spin echo of spins diffusing in a bounded medium. J Chem Phys. 1974;4508(August):4508-4511. doi:10.1063/1.1680931

36. Reynaud O, Winters KV, Hoang DM, Wadghiri YZ, Novikov DS, Kim SG. Pulsed and oscillating gradient MRI for assessment of cell size and extracellular space (POMACE) in mouse gliomas. NMR Biomed. 2016;29(10):1350-1363. doi:10.1002/nbm.3577

37. Novikov DS, Jensen JH, Helpern JA, Fieremans E. Revealing mesoscopic structural universality with diffusion. Proceedings of the National Academy of Sciences. 2014;111(14):5088-5093. doi:10.1073/pnas.1316944111

38. Harkins KD, Galons JP, Secomb TW, Trouard TP. Assessment of the effects of cellular tissue properties on ADC measurements by numerical simulation of water diffusion. Magn Reson Med. 2009;62(6):1414-1422. doi:10.1002/mrm.22155

39. Stepišnik J. Analysis of NMR self-diffusion measurements by a density matrix calculation. Physica B+C. 1981;104(3):350-364. doi:10.1016/0378-4363(81)90182-0

40. Assaf Y, Freidlin RZ, Rohde GK, Basser PJ. New modeling and experimental framework to characterize hindered and restricted water diffusion in brain white matter. Magn Reson Med. 2004;52(5):965-978. doi:10.1002/mrm.20274

41. Alexander DC, Dyrby TB, Nilsson M, Zhang H. Imaging brain microstructure with diffusion MRI: practicality and applications. NMR Biomed. 2019;32(4). doi:10.1002/nbm.3841

42. Kerkelä L, Nery F, Hall M, Clark C. Disimpy: A massively parallel Monte Carlo simulator for generating diffusion-weighted MRI data in Python. J Open Source Softw. 2020;5(52):2527. doi:10.21105/joss.02527

43. Johnston EW, Bonet-Carne E, Ferizi U, et al. VERDICT MRI for prostate cancer: Intracellular volume fraction versus apparent diffusion coefficient. Radiology. 2019;291(2):391-397. doi:10.1148/radiol.2019181749

44. Palombo M, Valindria V, Singh S, et al. Joint estimation of relaxation and diffusion tissue parameters for prostate cancer with relaxation-VERDICT MRI. Sci Rep. 2023;13(1). doi:10.1038/s41598-023-30182-1

45. Sen S, Valindria V, Slator PJ, et al. Differentiating False Positive Lesions from Clinically Significant Cancer and Normal Prostate Tissue Using VERDICT MRI and Other Diffusion Models. Diagnostics. 2022;12(7). doi:10.3390/diagnostics12071631

46. Srinivasan A, Galbán CJ, Johnson TD, Chenevert TL, Ross BD, Mukherji SK. Utility of the K-means clustering algorithm in differentiating apparent diffusion coefficient values of benign and malignant neck pathologies. American Journal of Neuroradiology. 2010;31(4):736-740. doi:10.3174/ajnr.A1901

47. Gray C, MacGillivray TJ, Eeley C, et al. Magnetic resonance imaging with k-means clustering objectively measures whole muscle volume compartments in sarcopenia/cancer cachexia. Clinical Nutrition. 2011;30(1):106-111. doi:10.1016/j.clnu.2010.07.012

48. Khan AR, Khan S, Harouni M, Abbasi R, Iqbal S, Mehmood Z. Brain tumor segmentation using K-means clustering and deep learning with synthetic data augmentation for classification. Microsc Res Tech. 2021;84(7):1389-1399. doi:10.1002/jemt.23694

49. Chan SW, Hu WH, Ouyang YC, et al. Quantitative Measurement of Breast Tumors Using Intravoxel Incoherent Motion (IVIM) MR Images. J Pers Med. 2021;11(7):656. doi:10.3390/jpm11070656

50. Campello RJGB, Moulavi D, Sander J. Density-based clustering based on hierarchical density estimates. In: Lecture Notes in Computer Science (Including Subseries Lecture Notes in Artificial Intelligence and Lecture Notes in Bioinformatics). Vol 7819 LNAI. ; 2013:160-172. doi:10.1007/978-3-642-37456-2_14

51. Campello RJGB, Moulavi D, Zimek A, Sander J. Hierarchical Density Estimates for Data Clustering, Visualization, and Outlier Detection. ACM Trans Knowl Discov Data. 2015;10(1):1-51. doi:10.1145/2733381

52. Von Luxburg U. A tutorial on spectral clustering. Stat Comput. 2007;17(4):395-416. doi:10.1007/s11222-007-9033-z

53. Lam WW, Oakden W, Karami E, et al. An Automated Segmentation Pipeline for Intratumoural Regions in Animal Xenografts Using Machine Learning and Saturation Transfer MRI. Sci Rep. 2020;10(1):1-14. doi:10.1038/s41598-020-64912-6

54. Jardim-Perassi B V., Huang S, Dominguez-Viqueira W, et al. Multiparametric MRI and Coregistered Histology Identify Tumor Habitats in Breast Cancer Mouse Models. Cancer Res. 2019;79(15):3952-3964. doi:10.1158/0008-5472.CAN-19-0213

55. Featherstone AK, O'Connor JPB, Little RA, et al. Data-driven mapping of hypoxia-related tumor heterogeneity using DCE-MRI and OE-MRI. Magn Reson Med. 2018;79(4):2236-2245. doi:10.1002/mrm.26860

56. Kölby L, Bernhardt P, Ahlman H, et al. A transplantable human carcinoid as model for somatostatin receptor-mediated and amine transporter-mediated radionuclide uptake. American Journal of Pathology. 2001;158(2):745-755. doi:10.1016/S0002-9440(10)64017-5

57. Chang SC, Lai PH, Chen WL, et al. Diffusion-weighted MRI features of brain abscess and cystic or necrotic brain tumors: Comparison with conventional MRI. Clin Imaging. 2002;26(4):227-236. doi:10.1016/S0899-7071(02)00436-9

58. Zhang Y, Chen J, Shen J, Zhong J, Ye R, Liang B. Apparent diffusion coefficient values of necrotic and solid portion of lymph nodes: Differential diagnostic value in cervical lymphadenopathy. Clin Radiol. 2013;68(3):224-231. doi:10.1016/j.crad.2011.04.002

59. Sharma U, Sah RG, Parshad R, Sharma R, Seenu V, Jagannathan NR. Role of apparent diffusion coefficient values for the differentiation of viable and necrotic areas of breast cancer and its potential utility to guide voxel positioning for MRS in the absence of dynamic contrast-enhanced MRI data. Magn Reson Imaging. 2012;30(5):649-655. doi:10.1016/j.mri.2012.02.009

60. Kroemer G, Galluzzi L, Vandenabeele P, et al. Classification of cell death: Recommendations of the Nomenclature Committee on Cell Death 2009. Cell Death Differ. 2009;16(1):3-11. doi:10.1038/cdd.2008.150

61. Nilsson M, Van Westen D, Ståhlberg F, Sundgren PC, Lätt J. The role of tissue microstructure and water exchange in biophysical modelling of diffusion in white matter. Magnetic Resonance Materials in Physics, Biology and Medicine. 2013;26(4):345-370. doi:10.1007/s10334-013-0371-x

62. Khan MKH, Guo W, Liu J, et al. Machine learning and deep learning for brain tumor MRI image segmentation. Exp Biol Med. 2023;248(21):1974-1992. doi:10.1177/15353702231214259

63. Balkenende L, Teuwen J, Mann RM. Application of Deep Learning in Breast Cancer Imaging. Semin Nucl Med. 2022;52(5):584-596. doi:10.1053/j.semnuclmed.2022.02.003

64. Quanyang W, Yao H, Sicong W, et al. Artificial intelligence in lung cancer screening: Detection, classification, prediction, and prognosis. Cancer Med. 2024;13(7):1-19. doi:10.1002/cam4.7140

65. Broggi G, Maniaci A, Lentini M, et al. Artificial Intelligence in Head and Neck Cancer Diagnosis: A Comprehensive Review with Emphasis on Radiomics, Histopathological, and Molecular Applications. Cancers (Basel). 2024;16(21). doi:10.3390/cancers16213623

66. Alexander DC, Dyrby TB, Nilsson M, Zhang H. Imaging brain microstructure with diffusion MRI: practicality and applications. NMR Biomed. 2019;32(4). doi:10.1002/nbm.3841

67. Fokkinga E, Hernandez-Tamames JA, Ianus A, et al. Advanced Diffusion-Weighted MRI for Cancer Microstructure Assessment in Body Imaging, and Its Relationship With Histology. Journal of Magnetic Resonance Imaging. 2023;60(4):1278-1304. doi:10.1002/jmri.29144

68. Hompland T, Hole KH kon, Ragnum HB, et al. Combined mr imaging of oxygen consumption and supply reveals tumor hypoxia and aggressiveness in prostate cancer patients. Cancer Res. 2018;78(16):4774-4785. doi:10.1158/0008-5472.CAN-17-3806

69. Xu J, Jiang X, Li H, et al. Magnetic resonance imaging of mean cell size in human breast tumors. Magn Reson Med. 2020;83(6):2002-2014. doi:10.1002/mrm.28056

70. Duchêne G, Abarca-Quinones J, Leclercq I, Duprez T, Peeters F. Insights into tissue microstructure using a double diffusion encoding sequence on a clinical scanner: Validation and application to experimental tumor models. Magn Reson Med. 2020;83(4):1263-1276. doi:10.1002/mrm.28012

71. Wu D, Jiang K, Li H, et al. Time-Dependent Diffusion MRI for Quantitative Microstructural Mapping of Prostate Cancer. Radiology. 2022;303(3):578-587. doi:10.1148/radiol.211180

72. Meyer HJ, Höhn AK, Woidacki K, et al. Associations between IVIM histogram parameters and histopathology in rectal cancer. Magn Reson Imaging. 2021;77(December 2020):21-27. doi:10.1016/j.mri.2020.12.008

73. Duchêne G, Abarca-Quinones J, Leclercq I, Duprez T, Peeters F. Insights into tissue microstructure using a double diffusion encoding sequence on a clinical scanner: Validation and application to experimental tumor models. Magn Reson Med. 2020;83(4):1263-1276. doi:10.1002/mrm.28012

74. Taqi S, Sami S, Sami L, Zaki S. A review of artifacts in histopathology. Journal of Oral and Maxillofacial Pathology. 2018;22(2):279. doi:10.4103/jomfp.JOMFP_125_15

75. Richardson S, Siow B, Panagiotaki E, Schneider T, Lythgoe MF, Alexander DC. Viable and fixed white matter: Diffusion magnetic resonance comparisons and contrasts at physiological temperature. Magn Reson Med. 2014;72(4):1151-1161. doi:10.1002/mrm.25012

76. Margarone JE, Natiella JR, Vaughan CD. Artifacts in oral biopsy specimens. Journal of Oral and Maxillofacial Surgery. 1985;43(3):163-172. doi:10.1016/0278-2391(85)90154-5

77. Cooper M, Ji Z, Krishnan RG. Machine learning in computational histopathology: Challenges and opportunities. Genes Chromosomes Cancer. 2023;62(9):540-556. doi:10.1002/gcc.23177

78. Berg S, Kutra D, Kroeger T, et al. ilastik: interactive machine learning for (bio)image analysis. Nat Methods. 2019;16(12):1226-1232. doi:10.1038/S41592-019-0582-9

79. Mancini M, Casamitjana A, Peter L, et al. A multimodal computational pipeline for 3D histology of the human brain. Sci Rep. 2020;10(1):1-21. doi:10.1038/s41598-020-69163-z

80. Zimmerman BE, Johnson SL, Odéen HA, et al. Histology to 3D in vivo MR registration for volumetric evaluation of MRgFUS treatment assessment biomarkers. Sci Rep. 2021;11(1):1-12. doi:10.1038/s41598-021-97309-0

81. Kerr JFR, Wyllie AH, Currie AR. Apoptosis: A Basic Biological Phenomenon with Wideranging Implications in Tissue Kinetics. Br J Cancer. 1972;26(4):239-257. doi:10.1038/bjc.1972.33

82. Hänggi K, Ruffell B. Cell death, therapeutics, and the immune response in cancer. Trends Cancer. 2023;9(5):381-396. doi:10.1016/j.trecan.2023.02.001

83. Galluzzi L, Vitale I, Aaronson SA, et al. Molecular mechanisms of cell death: Recommendations of the Nomenclature Committee on Cell Death 2018. Cell Death Differ. 2018;25(3):486-541. doi:10.1038/s41418-017-0012-4

84. Galbán CJ, Hoff BA, Chenevert TL, Ross BD. Diffusion MRI in early cancer therapeutic response assessment. NMR Biomed. 2017;30(3). doi:10.1002/nbm.3458

85. Surov A, Meyer HJ, Wienke A. Correlation between apparent diffusion coefficient (ADC) and cellularity is different in several tumors: a meta-analysis. Oncotarget. 2017;8(35):59492-59499. doi:10.18632/oncotarget.17752

86. Longo DL, Dastrù W, Consolino L, et al. Cluster analysis of quantitative parametric maps from DCE-MRI: Application in evaluating heterogeneity of tumor response to antiangiogenic treatment. Magn Reson Imaging. 2015;33(6):725-736. doi:10.1016/j.mri.2015.03.005

87. Borri M, Schmidt MA, Powell C, et al. Characterizing heterogeneity within head and neck lesions using cluster analysis of multi-parametric MRI data. PLoS One. 2015;10(9):1-13. doi:10.1371/journal.pone.0138545

88. Veraart J, Novikov DS, Fieremans E. TE dependent Diffusion Imaging (TEdDI) distinguishes between compartmental T2 relaxation times. Neuroimage. 2018;182(April 2017):360-369. doi:10.1016/j.neuroimage.2017.09.030

89. Qin W, Yu CS, Zhang F, et al. Effects of echo time on diffusion quantification of brain white matter at 1.5T and 3.0T. Magn Reson Med. 2009;61(4):755-760. doi:10.1002/mrm.21920

90. Gong T, Tong Q, He H, Sun Y, Zhong J, Zhang H. MTE-NODDI: Multi-TE NODDI for disentangling non-T2-weighted signal fractions from compartment-specific T2 relaxation times. Neuroimage. 2020;217(January):116906. doi:10.1016/j.neuroimage.2020.116906

91. Johansson J, Lagerstrand K, Björkman-Burtscher IM, Laesser M, Hebelka H, Maier SE. Normal Brain and Brain Tumor ADC: Changes Resulting From Variation of Diffusion Time and/or Echo Time in Pulsed-Gradient Spin Echo Diffusion Imaging. Invest Radiol. 2024;59(10):727-736. doi:10.1097/RLI.0000000000001081

92. Afzali M, Pieciak T, Newman S, et al. The sensitivity of diffusion MRI to microstructural properties and experimental factors. J Neurosci Methods. 2021;347(September 2020). doi:10.1016/j.jneumeth.2020.108951

93. Jelescu IO, Palombo M, Bagnato F, Schilling KG. Challenges for biophysical modeling of microstructure. J Neurosci Methods. 2020;344(July):108861. doi:10.1016/j.jneumeth.2020.108861

94. Lampinen B, Szczepankiewicz F, Lätt J, et al. Probing brain tissue microstructure with MRI: principles, challenges, and the role of multidimensional diffusion-relaxation encoding. Neuroimage. 2023;282(February). doi:10.1016/j.neuroimage.2023.120338

95. Veraart J, Novikov DS, Fieremans E. TE dependent Diffusion Imaging (TEdDI) distinguishes between compartmental T2 relaxation times. Neuroimage. 2018;182(April 2017):360-369. doi:10.1016/j.neuroimage.2017.09.030

96. White NS, McDonald C, Farid N, et al. Diffusion-weighted imaging in cancer: physical foundations and applications of restriction spectrum imaging. Cancer Res. 2014;74(17):4638-4652. doi:10.1158/0008-5472.CAN-13-3534

97. Novikov DS, Fieremans E, Jespersen SN, Kiselev VG. Quantifying brain microstructure with diffusion MRI: Theory and parameter estimation. NMR Biomed. 2019;32(4):1-53. doi:10.1002/nbm.3998

98. Mitra PP, Sen PN, Schwartz LM. Short-time behavior of the diffusion coefficient as a geometrical probe of porous media. Phys Rev B. 1993;47(14):8565-8574. doi:10.1103/PhysRevB.47.8565

99. Parsons EC, Does MD, Gore JC. Temporal diffusion spectroscopy: Theory and implementation in restricted systems using oscillating gradients. Magn Reson Med. 2006;55(1):75-84. doi:10.1002/mrm.20732

100. Wang X, Du L, Cao Y, et al. Comparing extracellular volume fraction with apparent diffusion coefficient for the characterization of breast tumors. Eur J Radiol. 2024;171(November 2023):111268. doi:10.1016/j.ejrad.2023.111268

101. Rafael-Patino J, Romascano D, Ramirez-Manzanares A, Canales-Rodríguez EJ, Girard G, Thiran JP. Robust Monte-Carlo Simulations in Diffusion-MRI: Effect of the Substrate Complexity and Parameter Choice on the Reproducibility of Results. Front Neuroinform. 2020;14(March). doi:10.3389/fninf.2020.00008

102. Rensonnet G, Scherrer B, Girard G, et al. Towards microstructure fingerprinting: Estimation of tissue properties from a dictionary of Monte Carlo diffusion MRI simulations. Neuroimage. 2019;184(May 2018):964-980. doi:10.1016/j.neuroimage.2018.09.076

103. Fang C, Yang Z, Wassermann D, Li JR. A simulation-driven supervised learning framework to estimate brain microstructure using diffusion MRI. Med Image Anal. 2023;90(September):102979. doi:10.1016/j.media.2023.102979

104. Jelescu IO, Palombo M, Bagnato F, Schilling KG. Challenges for biophysical modeling of microstructure. J Neurosci Methods. 2020;344(April):108861. doi:10.1016/j.jneumeth.2020.108861

105. Wang J, Hesketh RL, Gore JC, Brindle KM. The need for evidence-based, outcome-focused medical imaging research for cancer management. npj Imaging. 2025;3(1):6. doi:10.1038/s44303-024-00067-7

106. Nilsson M, Lasič S, Drobnjak I, Topgaard D, Westin CF. Resolution limit of cylinder diameter estimation by diffusion MRI: The impact of gradient waveform and orientation dispersion. NMR Biomed. 2017;30(7):1-13. doi:10.1002/nbm.3711

107. Vachha B, Huang SY. MRI with ultrahigh field strength and high-performance gradients: challenges and opportunities for clinical neuroimaging at 7 T and beyond. Eur Radiol Exp. 2021;5(1). doi:10.1186/s41747-021-00216-2

108. Gudino N, Littin S. Advancements in Gradient System Performance for Clinical and Research MRI. Journal of Magnetic Resonance Imaging. 2023;57(1):57-70. doi:10.1002/jmri.28421

109. Nilsson M, Lätt J, van Westen D, et al. Noninvasive mapping of water diffusional exchange in the human brain using filter-exchange imaging. Magn Reson Med. 2013;69(6):1572-1580. doi:10.1002/mrm.24395

110. Tang L, Zhou XJ. Diffusion MRI of cancer: From low to high b-values. Journal of Magnetic Resonance Imaging. 2019;49(1):23-40. doi:10.1002/jmri.26293

111. Li H, Jiang X, Xie J, McIntyre JO, Gore JC, Xu J. Time-Dependent Influence of Cell Membrane Permeability on MR Diffusion Measurements. Magn Reson Med. 2016;75(5):1927-1934. doi:10.1002/mrm.25724

112. Sen S, Singh S, Pye H, et al. ssVERDICT: Self-supervised VERDICT-MRI for enhanced prostate tumor characterization. Magn Reson Med. 2024;92(5):2181-2192. doi:10.1002/mrm.30186

113. Alemany I, Rose JN, Garnier-Brun J, Scott AD, Doorly DJ. Random walk diffusion simulations in semi-permeable layered media with varying diffusivity. Sci Rep. 2022;12(1). doi:10.1038/s41598-022-14541-y

114. Callaghan R, Alexander DC, Palombo M, Zhang H. ConFiG: Contextual Fibre Growth to generate realistic axonal packing for diffusion MRI simulation. Neuroimage. 2020;220(March):117107. doi:10.1016/j.neuroimage.2020.117107

115. Mushtaha FN, Kuehn TK, El-Deeb O, et al. Design and characterization of a 3D-printed axon-mimetic phantom for diffusion MRI. Magn Reson Med. 2021;86(5):2482-2496. doi:10.1002/mrm.28886